NATIONAL TECHNICAL UNIVERSITY OF ATHENS

SCHOOL OF NAVAL ARCHITECTURE & MARINE ENGINEERING

DEPARTMENT OF MARINE AND NAVAL HYDRODYNAMIC

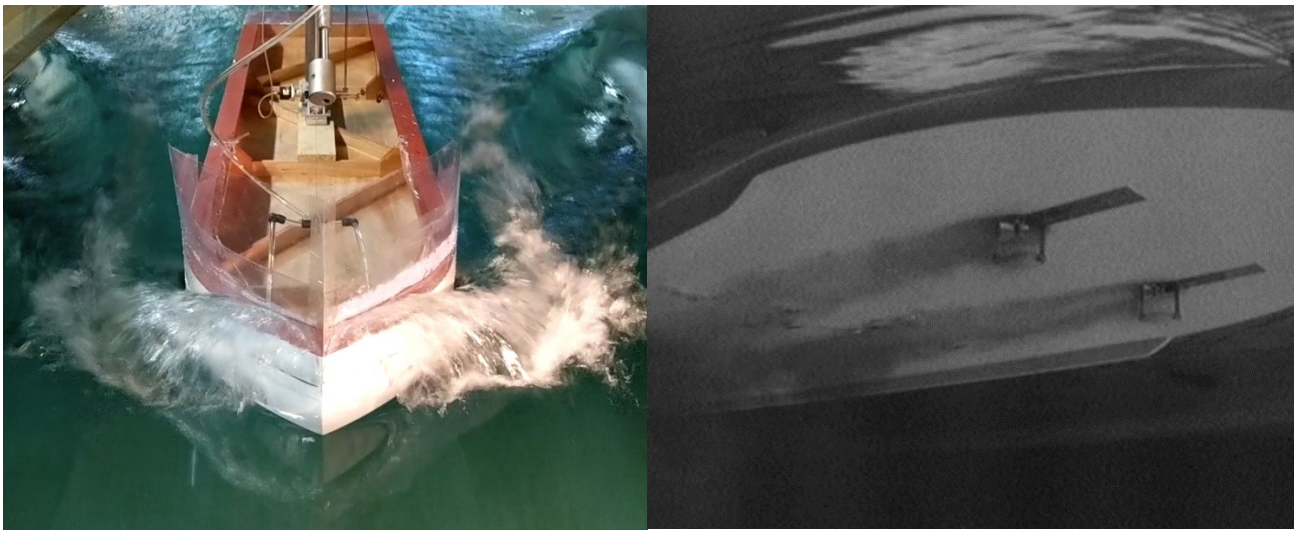

Experimental Investigation of the Effect of Superhydrophobic Coating and Microbubbles Lubrication on the Resistance of a Scaled Ship Model

Diploma Thesis

Athens, September 2019

Author : Paul Lee

Supervisor : G. S. Triantafyllou, Professor, NTUA

ABSTRACT

Skin friction of a fluid flowing near a solid surface poses many problems in variety applications. Increased energy consumption in marine and aerospace vehicles and decreased performances in hydraulic systems are one of the major issues to name a few. Thus, reduction of frictional drag leads to obvious technological advantages from an engineering perspective with additional economical and environmental benefits. Various studies and intense research have been conducted by the scientific community in order to propose effective ways to reduce frictional drag. Few of the many techniques are the reduction of resistance through super water repellent coatings, also known as superhydrophobic, and microbubble injection in the boundary layer. In this thesis, the effectiveness of the aforementioned techniques is tested experimentally by comparing the total resistance of a ship model with and without the introduction of microbubbles under the condition of a superhydrophobic coated surface in order to examine the performance difference between them. The flat of bottom of a 2.52 [m] long ship model is treated with a special nano-ceramic coating and a microbubble generator attached on the stem is able to produce fine bubbles of 50 [μm] diameter. The total resistance is recorded at towing speeds of 1.5, 2.0, and 2.5 [m/s], at an even keel and 0.5^{o} trim by stern condition, and a maximum of 4.5% reduction of the frictional coefficient is noted.

This paper is divided into four chapters. The 1st chapter provides an introduction to the skin friction problem in maritime, a literature review, and a proposal of an experimental concept. Chapter 2 provides details of the microbubble generator and its setup while chapter 3 presents the implementation of the experimental concept and necessary optimizations. Analysis of the measurements data are presented in the last chapter with final notes.

Key words

Frictional Drag Reduction; Microbubble Lubrication; Superhydrophobic Coating

ACKNOWLEDGEMENTS

This work is part of the undergraduate thesis of the author of this paper. The present diploma thesis is completing a five-year period of studies and research at the School of Naval Architecture and Marine Engineering of National Technical University of Athens. Taking this opportunity the author would like to express his sincere gratitude to God first and to all the members of the Department and Laboratory of Marine and Naval Hydrodynamics, whose contribution were valuable in accomplishing this work.

The author would like to acknowledge Professor G. S. Triantafyllou's significant contribution in conducting this research. The author would like to express his deepest gratitude for his willingness to give the opportunity to the author and supervise his work by providing valuable insights, guidelines, and mentoring in conducting the experiments and writing the thesis. The author is grateful to Professor G. S. Triantafyllou's open-mindedness in pioneering a new research of its kind in the faculty and for his trust towards the author and the staff members of the Laboratory to accomplish an experiment of high complexity and shed light in this field. Because of his contribution the Department of Naval and Marine Hydrodynamics were able to pioneer a resistance experiment with microbubble injection.

The author would like to express his sincere gratitude to Prof. G. Tzampiras, who is the head Director of the Marine and Naval Hydrodynamic Laboratory, for his significant contribution in receiving all the necessary funds for the experimental equipment. The author is grateful for his general directions, for his consideration towards the needs of the experiment, and for providing the Laboratory for 4 months in order to conduct all the necessary experiments.

The author wishes to acknowledge the significant contribution of all staff members of the Marine and Naval Hydrodynamic Laboratory who were engaged in this research and did their best in accomplishing this work. Specifically, the author would like to express his gratitude to Mr. Liarokaptis, for his useful remarks and counseling from start to finish, from designing the experiment to analyzing and presenting the experimental results in precision. The author would like to express his gratitude to Mr. Trachanas, for his excellence in conducting measurements of high precision, for his great experience in managing the measuring instruments and electric circuits of the towing carriage, and for his crucial remarks during the measurements and affable character elevating the overall atmosphere. The author would like to express his gratitude to Mr. Milonas, for his contribution in 3D modeling and building the ship model, for letting the author assist during his work at the carpentry of the laboratory, and for his creativeness in proposing unique patents fitting to the specific needs of the experiment. Last but not lease, the author is also grateful to the company Ceramic Pro© for their offer to apply their unique superhydrophobic nano-ceramic coating free of charge considering its research purposes.

TABLE OF CONTENTS

INTRODUCTION

In this chapter, the idea of frictional drag reduction through the lubrication of microbubbles is introduced. In the first part, an introduction to the frictional drag and its effect in the marine transportation business is presented. In the second part, a literature review and an overview of the basic principles and physics of this phenomena with conclusive explanations are presented. In the last part, a basic concept for an experimental investigation is proposed in order to test, examine, and verify the relation between the frictional drag reduction and microbubble lubrication.

1.1 Introduction to the Problem

Commercial ships are of great importance in worldwide transportations. The marine transportation business relies heavily on such means as they play a primary role in transporting heavy loads such as crude oil, ore, and grain. In general, the ship resistance can be divided into two main components: the frictional drag, known as skin or viscous friction, and the residuary component. Due to the immense size and very slow speeds of such vehicles the residuary drag components, such as the free-surface wave resistance which is proportional to the square of the speed, are very small, whereas, the frictional drag which dominates at low Froude numbers and is proportional to the wetted surface area, can reach up to 80% of the total resistance (60-70% in cargo ships, 80% in tankers).

The reduction of the frictional drag has been a critical precondition in the marine transportation business, as it occupies an overwhelming percentage of the total drag resulting in serious economic and environmental issues. Approximately, 60% of a typical ship's propulsive power is known to be required to overcome frictional drag which translates into more required propulsive power and consequently more fuel consumption and gas pollutant emission. Fuel expenses represent the largest portion of a ship's total operation cost urging ship owners to find new techniques to save energy and reduce its consumptions. Regarding the environmental impact, based on a relevant report, ship engines in maritime transport are responsible for the 7% and 4% of total NO_X and SO_X contaminants emission, respectively, in the entire world, posing an increasingly serious problem to the greenhouse effect (Watanabe, 1991)**.** Hence, IMO has declared ever more strict regulations and guidelines to further reduce greenhouse gas emission by 2020 (Report of the Marine Environment Protection Committee on its Fifty-Eighth Session, 2008) pushing the marine industry and the scientific community on the verge to develop substantially energy efficient techniques or practices.

The reduction of frictional drag through the lubrication of microbubbles is among the many investigated and tested techniques with promising results. This technique lies in the simple idea of injecting microbubbles into the boundary layer formed on the submerged hull surface and thus reducing its frictional drag. This idea aroused the interest of the scientific community and many experiments with different approaches were conducted throughout the past centuries in order to confirm its effectiveness, investigate the basic physics of this technique, and give conclusive explanations of its complex mechanism.

1.2 Hull Resistance Components

The resistance of a ship is the force required to tow the ship in a calm water at a specific speed (Molland, Turnock, & Hudson, 2017). In order to understand how the energy of the ship's engine dissipates while moving through the water, its resistance components should be examined. When a hull moves through the water generation of wave patterns and vorticity can be noted indicating the energy dissipation from the ship to the surrounding water in a form of disturbance (see Fig. 1). A possible physical breakdown of resistance in terms of forces acting could be:

Frictional resistance The sum of all the tangential shear forces τ acting on the wetted surface of the hull due to the viscosity of the liquid projected at the direction of towing produces the frictional resistance (see Fig. 2).

Pressure resistance The sum of all normal wave pressure forces P distributed on the wetted surface of the hull due to in part to viscous effect and to hull wavemaking projected at the towing direction produces the total pressure resistance (see Fig. 2).

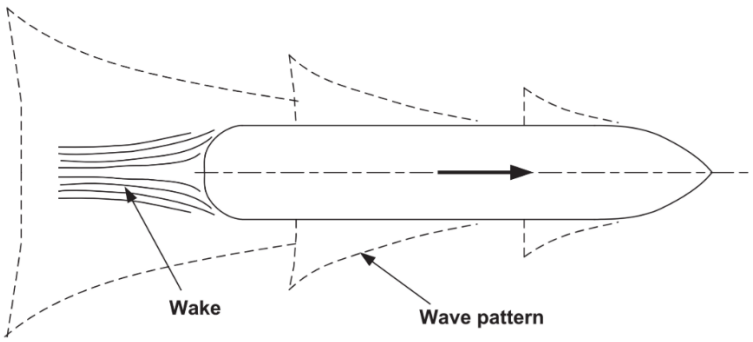

Figure 1 *Two basic forms of energy dissipation from a ship's hull into a liquid.*

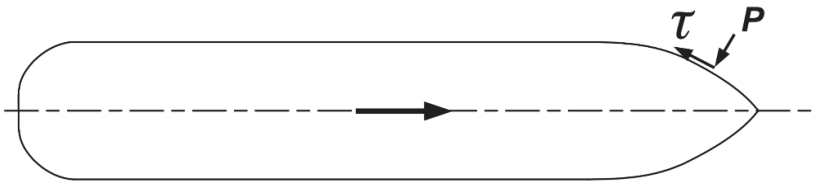

Figure 2 *Frictional and pressure forces acting upon a ship's hull.*

Another decomposition of the total resistance in terms of energy dissipation could be:

Total viscous resistance The energy lost to produces vorticity such as turbulence and wake vortices due to the the existence of viscosity and pressure loss due to flow separation in the behind the hull are equal to the total viscous resistance (see Fig. 3).

Total wave resistance The energy needed to produce the wave patterns in the free surface is equal to the total wave resistance.

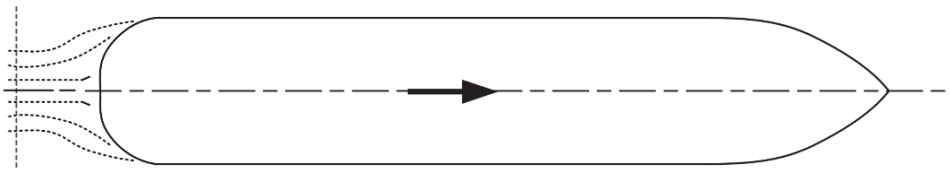

Figure 3 *Total viscous resistance acting upon a ship's hull.*

Other forces may also be present producing the residual resistances such as the air resistance, wave breaking resistance, added resistance in waved due to the interaction of the hull with incoming waves, added resistance due to turning, induced drag, and appendage resistance. A summary of these basic hydrodynamic components of the ship resistance is shown in Figure 4 while a more detailed decomposition with other contributing components is shown in Figure 5.

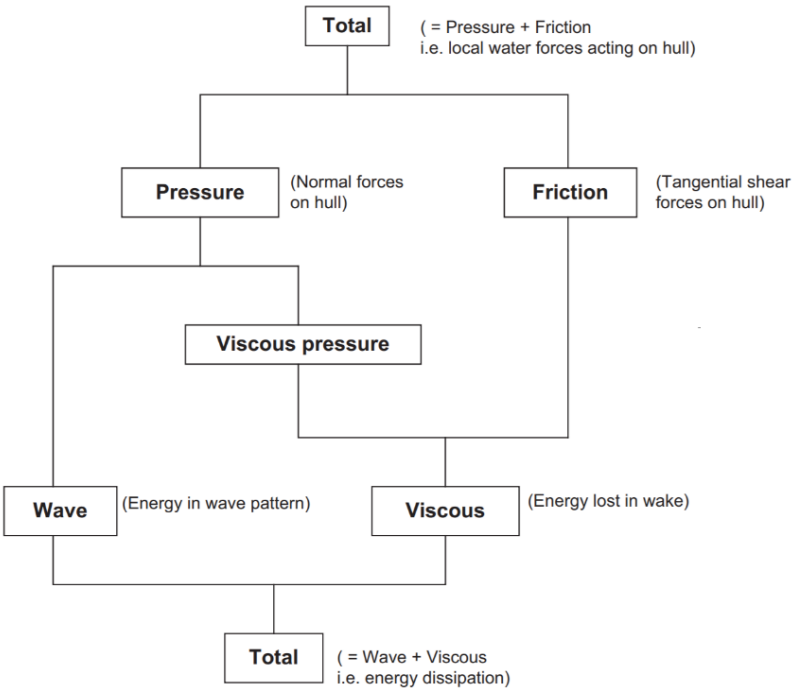

Figure 4 *Basic hydrodynamic components of a ship resistance.*

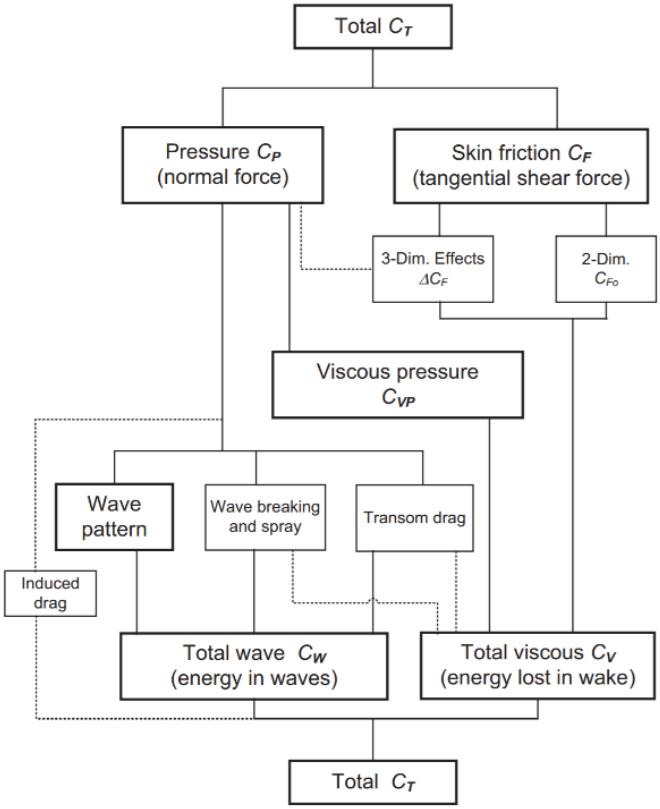

Figure 5 *Detailed hydrodynamic components of a ship resistance.*

1.3 Boundary Layer

In fluid mechanics, the concept of a “boundary layer” plays a major role in understanding and interpreting the complex mechanism and interaction between a solid surface and a fluid when in contact (Schlichting & Gersten, 1960). In a real fluid, particles of the fluid that comes in contact with the surface do not slip along the surface but rather adheres to it creating tangential forces, also known as shear forces, both between layers in the fluid and between the fluid and the wall. These frictional forces, which are significant, are directly related to the physical properties of the fluid, the viscosity, which is predominantly a function of the temperature. Viscosity of liquids are known to decrease with the increase of temperature, whereas the opposite is true in gases.

This transition from zero velocity at the surface to the full velocity occurs in a very thin layer called boundary layer or frictional layer. Simply put, a fluid flow can be divided up into two distinguished areas: 1) the boundary layer, which is a very thin layer close to the surface and dominated by viscosity creating the majority of the frictional drag, and 2) the outer flow area outside of the boundary layer where the viscosity can be neglected. There are two different types of boundary layer flow: laminar and turbulent. The laminar boundary is mainly characterized by a very smooth flow, while the turbulent boundary layer contains swirls or "eddies”. From a drag standpoint the laminar flow creates less skin friction drag than the turbulent flow, but is less stable.

Laminar Boundary Layer At low velocities, when the Reynolds number is below the critical value, Re_{crit} ~=3 10^6, the flow of the fluid is characterized by a laminar boundary layer, which has a “layered” profile as the fluid’s velocity alters perpendicular to the flow direction from the surface’s velocity, due to the no-slip condition, to the outer velocity of the flow. The thickness of the boundary layer $\delta(x)$ is usually defined as δ_{99} which is the point where the velocity reaches 99% of the outer velocity U_∞ and its thickness increases throughout the length (see Fig. 6). Most of the shear stress or frictional forces occur in the leading edge, where the particles of the fluid are forced to slow down and change their kinetic status. This accumulation of the slow downed particles of the fluid increases further downstream as the outer fluid constantly supplies the boundary layer. As a result, the thickness of the boundary layer increases and the effect of viscosity decreases monotonically downstream. The thickness of the boundary layer can become thinner at higher Reynolds number or with smaller viscosity fluids since the viscosity causes a momentum transport moving outwards from the wall.

Boundary Layer Transition The flow profile of a smooth laminar boundary layer swifts when the Reynolds number becomes greater than Re_{crit} with the increase of flow velocity. Then a transition of the laminar boundary layer of the leading edge into a turbulent boundary layer occurs downstream occurs together with a strong increase of the boundary layer’s thickness (see Fig. 7). This transition effect depends on many parameters apart from the Reynolds number, such as the pressure distribution of the outer flow, the surface’s roughness, and the level of disturbance of the outer flow. In the transition region where instabilities are dominant, the velocity fluctuations demonstrate the characteristic signal of periodic Tollmien–Schlichting waves. Next to that region, spikes create the local high shearing regions with lifting velocity profiles which further downstream increase in number until developing a fully irregular turbulent region. Numerical simulation results suggest that the magnitude of the shearing grows mostly in the spike area and that the region of high shearing appear close to the surface. One interesting manipulation of boundary layer transition is the use of a thin wire, also known as trip wire or turbulence stimulator that artificially makes the laminar flow turbulent at a lower Reynolds number in order to avoid flow separation. Flow separation can result in a great change in the pressure distribution downstream increasing the pressure drag. By placing a turbulence stimulator at the right place the separation

of the flow moves further downstream since the instability of the laminar leading to separation is now stabilized as the outer flow energizes the boundary layer in larger scale through the turbulent mixing motion.

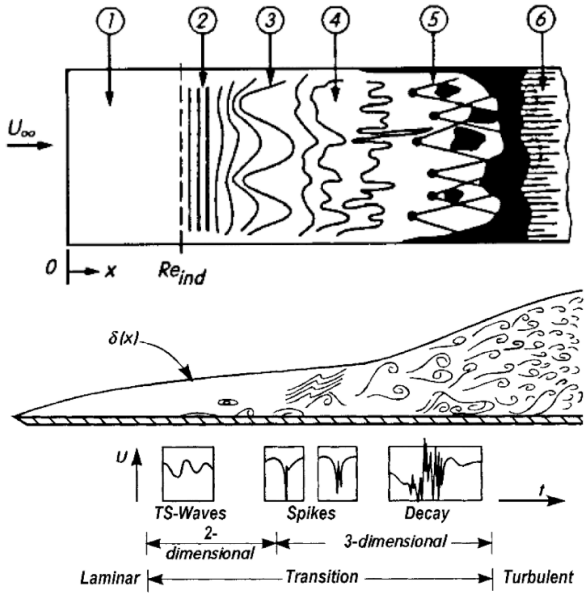

Figure 6 *Schematic boundary layer's transition: (1) stable laminar flow, (2) unstable Tollimien-Sclichting waves, (3) three-dimensional waves and vortex formation (Λ-structures), (4) vortex decay, (5) formation of turbulent spots, (6) fully turbulent flow.*

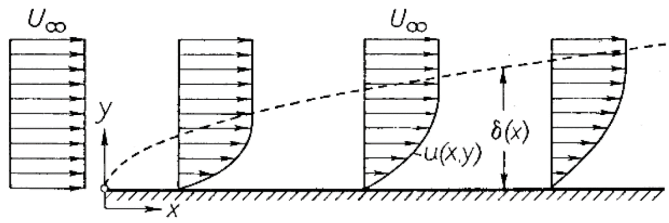

Figure 7 *Schematic representation of the velocity distribution in the laminar boundary layer.*

Turbulent Boundary Layer Usually turbulent flow occurs in most applications and a firm understanding of its mechanisms and components are necessary. This highly irregular flow characterized by random fluctuating motions is known as turbulent boundary layer where transverse movements are superimposed on the main motion in the direction of the flat surface exchanging momentum in the perpendicular direction. Unlike in the case of laminar boundary layer where the whole region is affect by the viscosity, in the turbulence case the boundary layer is divided into to sublayers: the turbulent layer, and the viscous sublayer. In the former layer only apparent friction forces occur due to turbulent fluctuating motions unaffected by its viscosity, whereas in the latter thinner layer the effects of the viscosity are present. The viscous sublayer consists of two parts, the linear sublayer closest to the surface, $y+ < 7$, and the buffer sublayer, $7 < y+ <40$, where the highly turbulence occurs. The thickness of the viscous sublayer decreases with the increase of Reynolds number.

One basic characteristic of a turbulent flow is that the velocity and pressure at a fixed point in space is not constant but rather fluctuates irregularly. The fluid elements carrying these kinetic fluctuations are macroscopic lumps of various sizes, known as eddies. Large eddies are constantly charged with energy from the outer flow entering the boundary layer, which in turn disseminate the energy into smaller eddies near the surface area until it dissipates completely. These eddies continually appear and disappear and their sizes varying from some tenths of a millimeter to several centimeters are determined by the external conditions of the flow. These fluctuating transverse motions of the eddies causes additional shear stress in the x direction on the surface, called apparent stress of the turbulent flow or Reynolds stress. More specifically transverse motions of the eddies lift particles of the flow from a lower layer to transfer their horizontal momentum of a lower average velocity while dragging downwards particles from an upper layer transferring their horizontal momentum of a higher average velocity. Reynolds stress, or the apparent stress of the turbulent flow becomes the dominant factor so that viscous stress can be neglected, unlike the sublayer. In other words, there is a correlation between the longitudinal and transverse fluctuations of the velocity at the same position.

1.4 Literature Review

Variety of applications, such as in marine, hydraulic, and aerospace, are interested in both passive and active means to reduce the frictional drag of a solid surface that is in contact with a fluid. Applying riblets and adding compliance to the surface, shaping and polishing the surface to maintain laminar flow to the greatest possible downstream are one of the methods that require no ongoing expenditure of energy, also known as fully passive methods. In contrast, fully active methods, such as transverse wall oscillations and electro-kinetic forcing of the near-wall flow, involve unsteady energy addition. A middle ground of these two methods are the techniques that involve a quasi-steady energy expenditure, such as the suction or blowing of the boundary layer, the injection of polymers or other non-Newtonian additives, and the injection of gas or bubbles into the boundary layer (Lumley, 1964; Sanders, Winkel, Dowling, Perlin, & Ceccio, 2006).

1.4.1 Microbubble Frictional Drag Reduction

The technique of frictional drag reduction through microbubble lubrication might be originated by the age-old idea of reducing the skin friction through a layer of air between a ship and its water boundary layer which was first patented in the 1800s (Crewe & Eggington, 1960). Though the instability of the air-liquid interface seemed to make the practicality of this technique questionable, the use of very fine bubbles seemed to offer alternative solutions to the interfacial instability while retaining many of the benefits of the original concept.

The first experimental work with microbubble frictional drag reduction was reported in 1973 when its reduction was tested on a 3-foot towed model wired around with copper producing hydrogen bubbles via electrolysis (Bhattacharrya & McCormick, 1973). During the experimental study five wire cathode configurations with various power supply and towing speeds were tested and the measured total drag were presented as a function of the towing speed with the electrical current as a parameter (see Fig. 8 & 9). It was found that towing speed and time-rate of hydrogen production which is proportional to the electrical current were the main parameters for the drag reduction that can be simplified to a single relevant parameter: the ratio of the mass flow of water within the wake to the time-rate of hydrogen mass produced beneath the boundary-layer. This conclusion was well confirmed when data were presented as a function of the latter parameter and collapsed to a line rather well (see Fig. 10). In lower speeds, where the boundary layer was laminar, drag reduction was estimated to be related with the increase in the curvature of the velocity profile in the presence of bubbles contributing to the stability of the laminar boundary layer due to the positive viscosity gradient near the wall as explained by (Lumley, 1964). When the boundary layer was turbulent the reduction of frictional drag was attributed to the disruption and possibly to the destruction of the laminar sublayer, eliminating the high shear region and thus reducing its frictional drag. Also bubbles' migration from the wall to outer regions of the boundary layer seemed to reduce turbulent stresses by absorbing the momentum with their elasticity while preventing the transmission of small viscous shear stresses from the turbulent areas to the wall due to their low viscosity. In contrast to the general trend, at some lower speeds a slight increase of frictional drag was noted in the presence of bubbles caused, possibly due to the presence of bubbles tripping the flow and causing the flow to become prematurely turbulent.

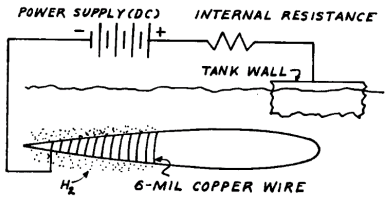

Figure 8 *Schematic diagram of electrolytic circuit and cathode orientation.*

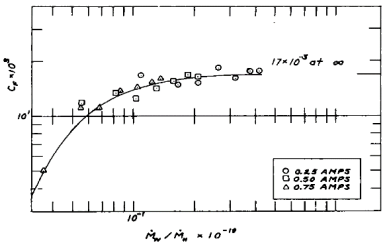

Figure 10 *Effect of H_2 mass production on the drag coefficient.*

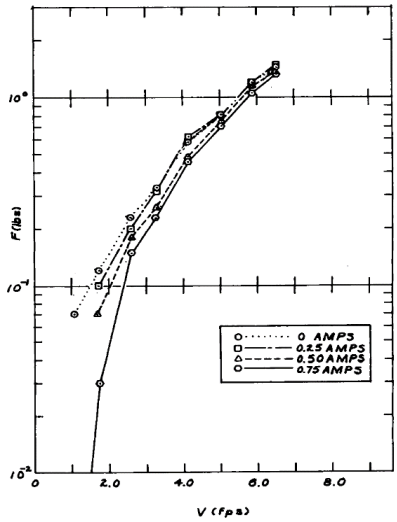

Figure 9 *Total resistance vs Towing speed.*

Based on the same frame, a more precise integrated and local skin friction measurements were conducted with the aim of documenting the range of parameters for which skin friction reduction can be observed (Madavan, Deutsch, & Merkle, 1984a; Madavan, Deutsch, & Merkle, 1984b; Madavan, Deutsch, & Merkle, 1985). The effect of buoyancy at different gravitational orientations, gas flow rate, freestream velocity, various porous material and sizes, and helium as ejectant instead of air, were tested on a rectangular test section wall of a water tunnel and a maximum reduction of 80% was observed (see Fig. 11). When plate-on-top, reduction in skin friction was noted as soon as the microbubbles were generated until reaching its minimum value (see Fig. 12). A more pronounced descrease in skin friction was present at lower tunnel velocities due to the increased volumetric concentration of air in the boundary layer compared at the higher speeds, as concluded in the prior work. Measurements taken with helium and air ejected through only the half of the porous section appeared to collapse when presented in terms of the volumetric fraction of air to water, indicating that the area of ejection and the mass concentration of the ejectant are not the relevant parameters, similar to the earlier statement (see Fig. 13). Also the types of porous surface and pore size ranging of 0.5-100 [μm] shown no substantial different in terms of drag redution and it was concluded that bubble size are not determined by the size of the pores but by the characteristcs of the flow. When plate-on-bottom, data taken from local skin friction measured no microbubble impingement indicating a bubble-free region close to the wall. In this orientation gravity entered as an additional parameter and no collapse of data was found when presented as a function of volumetric fraction of air to water, unlike the previous plate orientation. Regarding the downstream persistence of the skin friction reduction greatest values were noted close to the porous section while a relaxation towards its undisturbed values was noted father downstream (plate-on-bottom: 35δ, plate-on-top: 60-70δ, see Fig. 14), due to the decrease of air content occurred both by the boundary-layer growth and bubble migration. LDA mean velocity profiles indicated no dramatic realignment of the characteristics of the outer boundary layer in the presence of microbubbles leading to the conclusion that the introduction of bubbles causes no major restructuring of the turbulent boundary layer but rather modification (see Fig. 15). Frequency information extracted from the hot-film signals showed reduction of the high-frequency contents and turbulence energy shifting toward lower frequencies when microbubbles were present in the near-wall turbulence structure (see Fig. 16). This trend was interpreted based on a mechanism similar to the polymer drag reduction (Lumley, 1964) which suggests a decrease in the turbulent Reynolds number through the increase in viscosity and decrease in density in the two-phase flow resulting in a thicker sublayer.

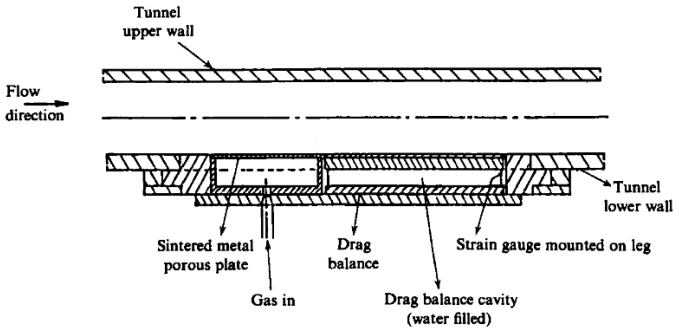

Figure 11 *Schematic of an experimental setup.*

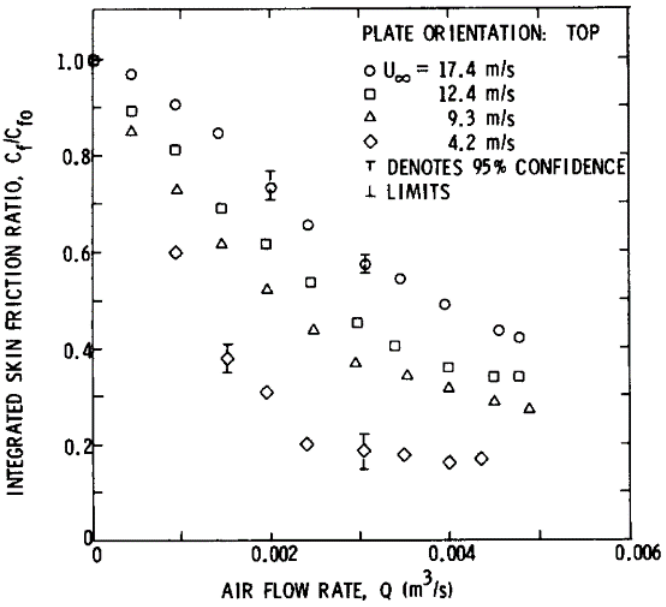

Figure 12 *Ratio of integrated skin friction in the presence of microbubbles to skin friction without microbubbles as a function of airflow rate. The plate is above the boundary layer.*

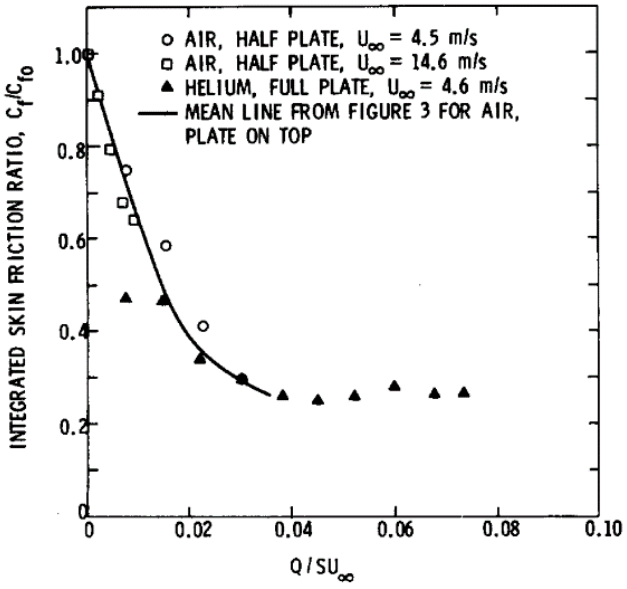

Figure 13 *Comparison of the effects of using helium instead of air as the injectant, and of using only half the porous plate. The plate is above the boundary layer.*

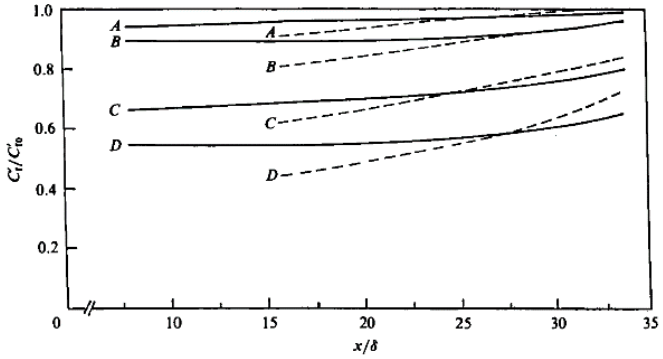

Figure 14 *The downstream persistence of the skin-friction reduction. Comparison of data taken with the plate above and below the boundary layer. U_∞ = 16.8 [m/s]. The solid line represents the plate on top, the dashed line the plate on bottom. $Q_a/(Q_a+Q_W)$ is 0.13 for A, 0.18 for B, 0.27 for C, and 0.34 for D.*

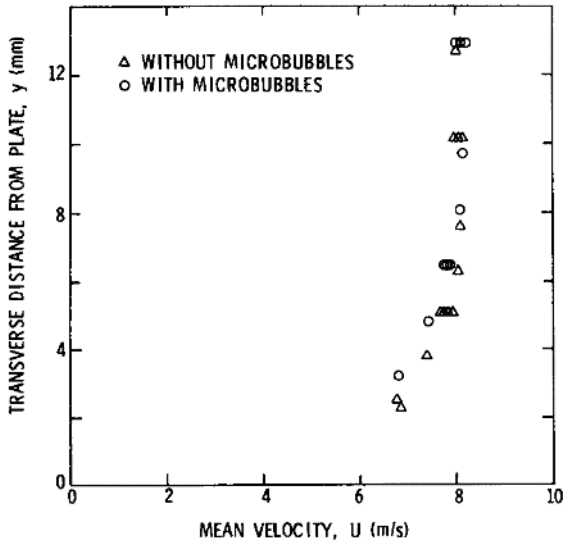

Figure 15 *Comparison of mean velocity profiles in outer part of boundary layer in the presence of microbubbles and in the absence of microbubbles.*

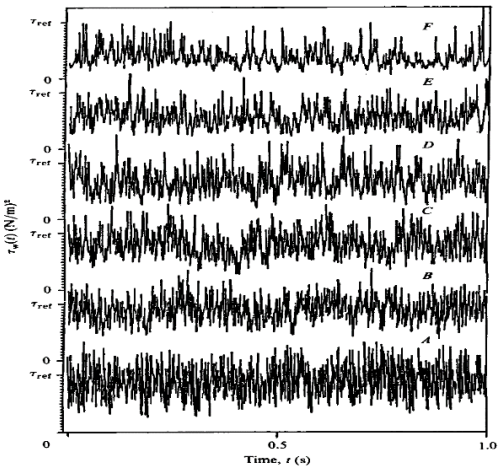

Figure 16 *A sequence of linearized hot-film signal traces in the presence and absence of microbubbles. A: no microbubbles; B: 10% air, 5% C_f reduction; C: 14% air, 15% C_f reduction; D: 19% air, 28% C_f reduction; E: 26% air, 40% C_f reduction; and F: 36% air, 62% C_f reduction.*

In 2006, surface shear stress and image-based measurements of near-wall bubble characteristics were conducted on a 12.9 [m] long flat-plate at Reynolds number as high as 2.1 10^8 in a recirculating water tunnel (Sanders, Winkel, Dowling, Perlin, & Ceccio, 2006). The test surface faced downward so that buoyancy would not enter as an added parameter and nominal speed of 6, 12, and 18 [m/s] were used. Air bubbles were injected through flush-mounted 40 [µm] strips at volumetric rates as high as 0.38 [m^3/s] and image-based measurements were conducted in order to determine the near-surface bubble characteristics, such as size, near-wall void fraction and distance, and convection speed. At the lowest speed and highest air injection rate, a nearly continuous gas film was formed beneath the test surface due to coalescence and buoyancy and frictional drag reduction reached nearly to 100%, whereas at the highest speeds, bubble images indicated that the bubbles generally remained distinct and increase in the reduction in skin friction with the increase of the area ratio was observed (see Fig. 17). Skin friction reduction of the air layer persisted further downstream of the air injector compared to the bubbly flow where it lasted only few meters forming a nearly bubble-free liquid layer, especially at higher flow speeds and larger bubbles. The persistence was limited due to the re-establishment of high shear at the surface producing shear-induced lift forces that act upon each discrete bubbles migrating them away from the near wall. Data taken out from skin friction ratio plotted as a function of image area ratio, which is monotonically proportional to the void fraction, revealed different flow speeds with similar area ratios producing substantially different drag reductions. This observation lead to the conclusion that bubbles in close proximity to the wall combined with large void fractions and small bubbles are the major factors corresponding to the generation of greater frictional drag reduction (see Fig. 18 & 19). From the same data it was also concluded that skin friction reduction is not merely an effect of reduced density since the high reduction of skin friction did not correspond with the same proportion in the reduction of near-wall density. As a result it was estimated that Reynolds shear stress in the boundary layer must be also attributed to the bubbles modifying the turbulent fluctuations, especially when bubble sizes are relevant to the smallest turbulence scales.

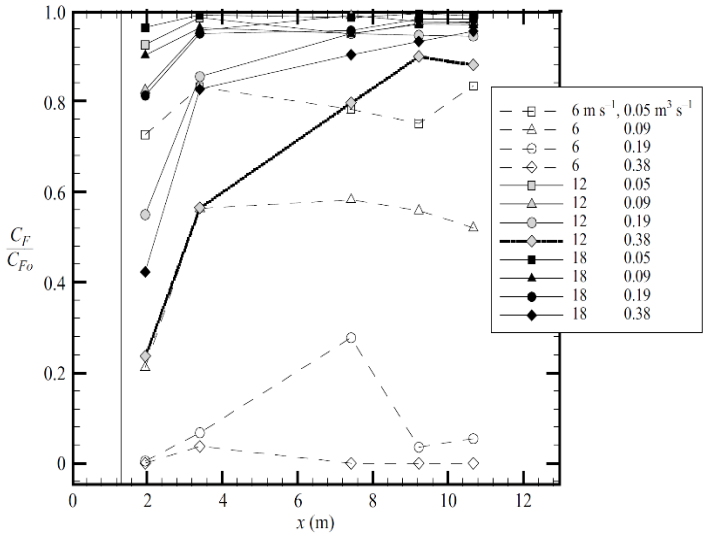

Figure 17 *Skin friction ratio C_F/C_{F0} as a function of downstream distance x (in metres) for upstream injection. Solid lines represent flow conditions having distince bubbles. Dashed lines represent flow conditions leading to a continueous or intermittent gas film.*

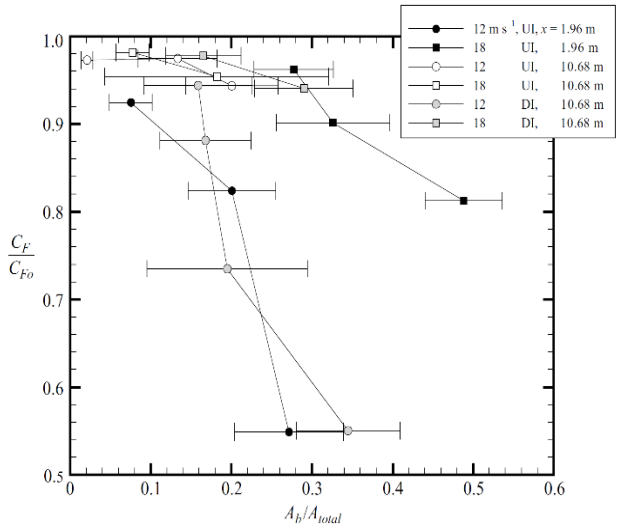

Figure 18 *The measured skin friction ratio as a function of the imaged area ratios. UI = upstream air injection at x = 1.32 [m]; DI = downstream air injection at x = 9.79 [m].*

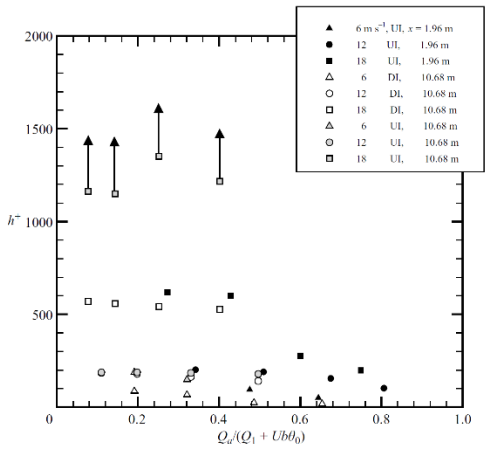

Figure 19 *Non-dimensional vertical distance, h^+, from the test surface to the bubbles nearest the test surface (bubbly flows) or to the air-water interface (gas-film flows) as a function of flux-based void fraction.*

In more recent years, an experimental characterization of the turbulent structure of a flat plate in the presence microbubbles, comparable with the local Kolmogorov lengthscale, was examined in a recirculating water channel (Jacob, Olivieri, Miozzi, Campana, & Piva, 2010). The plate was 6 [m] long and microbubbles of an average diameter 150 [μm] were produced by electrolysis with void fraction of 0.1% drifting toward the plate owing to buoyancy for constant freestream speeds of 0.75 and 1.0 [m/s] (see Fig. 20). A maximum reduction in drag up to 10% was measured (see Fig. 21). Optical image-processing techniques were used to acquire the bubble characteristics concentration fields (see Fig. 22 & 23). The zero bubble concentration in the wall seemed to occur due to turbulence and repulsive forces near the wall reducing bubbles' buoyancy rise velocities and migrating them into low-pressure areas or down-flow region of vortices. Maximum void fraction was presented to be at $D^+ = 5$ which corresponds to twice the local Kolmogorov lengthscale. Peak concentration in wall distance at $y^+ = 25$ indicated that bubbles accumulate preferably within the buffer region, where the most intense turbulent activity takes place. Similar to prior conclusions, the negligible void fraction of 0.1% in relation with the local reduction of skin-friction coefficient of 25% could not be accounted for only by the variations in fluid properties leading to the credence of bubbles' significant impact on the turbulent structure. Velocity measurements focused on the comparison of the mean velocity profile with and without bubbles clearly showed lower velocities close to the wall until the buffer region in the case with bubbles indicating a substantial decrease of the mean wall stress $\tau_w = \mu\,(\partial U/\partial y)|_w$ (see Fig. 24). Also, a pronounced modification in the Reynolds stress profile was noted, especially in the inner region, due to the decrease of the coherence of near-wall structures induced by the bubble forcing leading to a substantial reduction of the momentum flux toward the wall (see Fig. 25). As a result, turbulent kinetic energy seemed to be redistributed at smaller scales reducing the lengthscale of the eddies, a mechanism which was in contrary to the thickening of the dominant structures observed in polymer drag reduction.

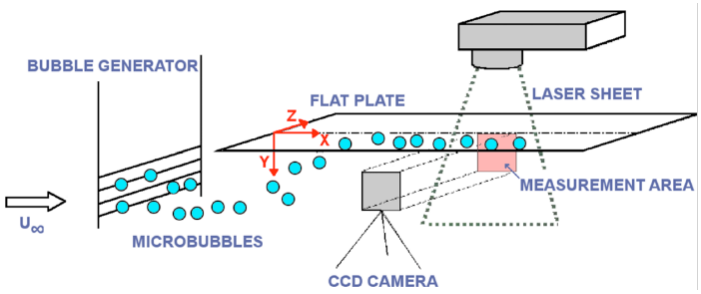

Figure 20 *Sketch of the experimental configuration.*

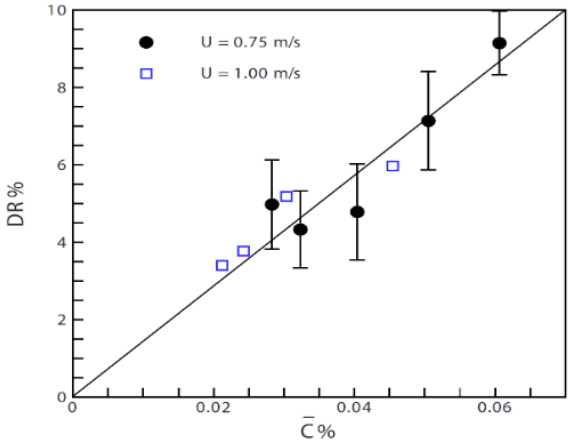

Figure 21 *The reduction of the frictional drag of a flat plate towed at constant speed U vs bulk void fraction C.*

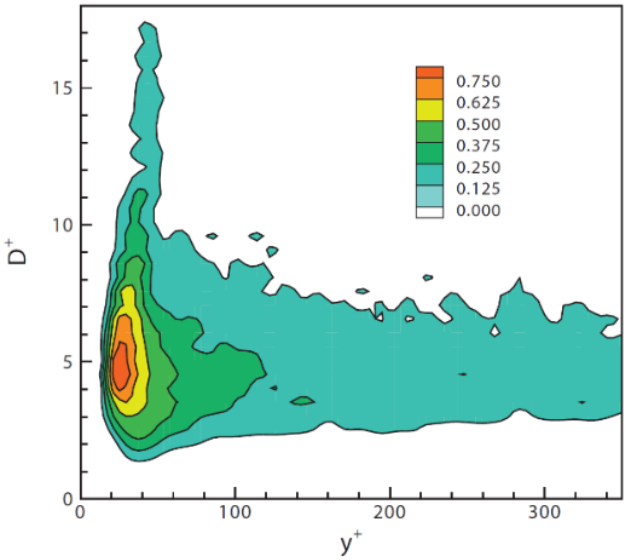

Figure 22 *The reduction of the frictional drag of a flat plate towed at constant speed U vs bulk void fraction C.*

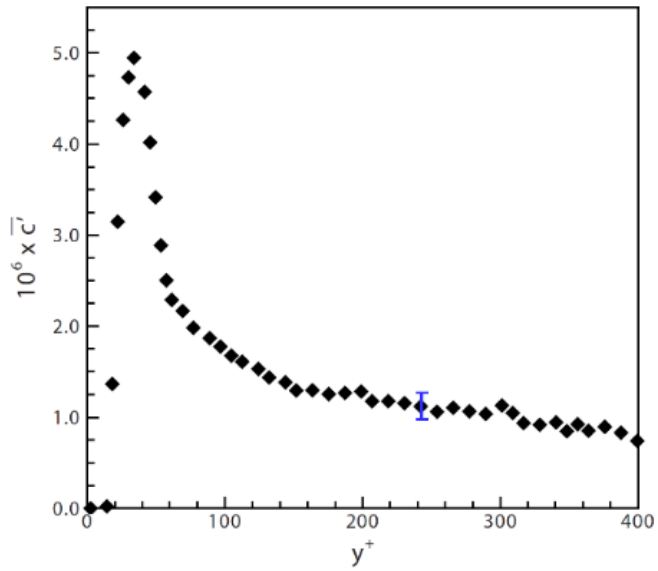

Figure 23 *The bubble concentration profile plotted as a function of the nondimensional wall-normal distance y⁺.*

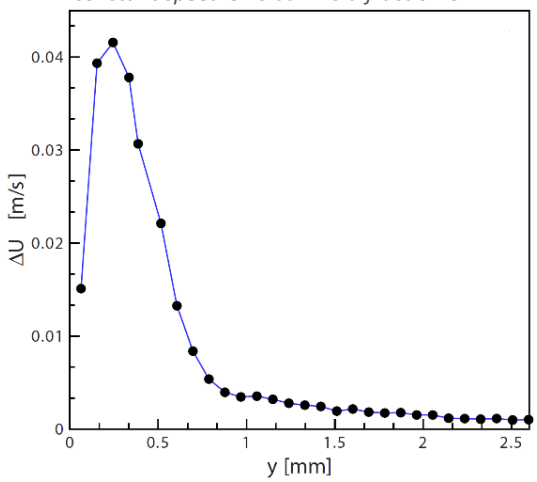

Figure 24 *Difference between the two velocity profiles as a function of wall distance. Note tat dimensional variables are used.*

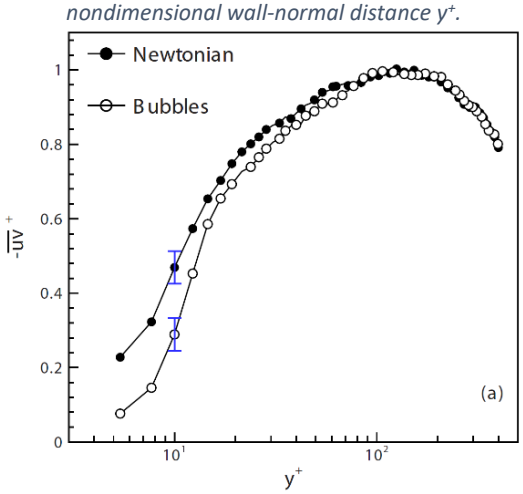

Figure 25 *Reynolds stress profiles for the Newtonian and the bubbly flows. Flow variables are normalized with the inner scales of the Newtonian flow.*

In 2016, further attempts to investigate the role of the bubbles in frictional drag reduction was done in a cavitation tunnel by visualizing the bubbly turbulent boundary layer on a surface of a flat plate (Paik, Yim, Kim, & Kim, 2016). Bubbles with mean diameter of 30-50 [μm] were released at a discharge flow rate of 5.77 [l/min] and at free velocity speeds of 1.0 to 3.0 [m/s]. Maximum skin friction reduction was noted to be 15% at flow speed of 1.5 [m/s] and a gradual reduction ratio decrease as the free flow speed increased occurred due to the reduction of the boundary layer's thickness corresponding to the reduction of the amount of microbubbles in the boundary layer (see Fig. 26). Flow visualization techniques were employed to determine the physical properties of the microbubbles in the wall boundary layer and a stratification not parallel to the wall was present in the two-phase flow unlike in the single phase flow (see Fig. 27). A comparison of the velocity characteristics in the boundary layer provided different velocity profiles in the buffer and inner layers (see Fig. 28). The distribution of the Reynolds stress values was examined and active turbulence production was observed in the buffer layer in the single phase flow, while decrease of the magnitude of Reynolds stress was observed when bubbles were introduced, leading to a reduction in turbulence production (see Fig. 29). More accurate visualization and comparisons of void fraction and concentration distributions of microbubbles concluded both local void fractions in the buffer layer and viscous sublayer lead to greater skin friction reductions. Relatively large fluctuation in vertical velocity in the buffer layer observed in velocity distribution measurements concluded that vertical motion of bubbles augment the reduction effect of skin friction as their vertical motions affect the longitudinal vortices (see Fig. 30).

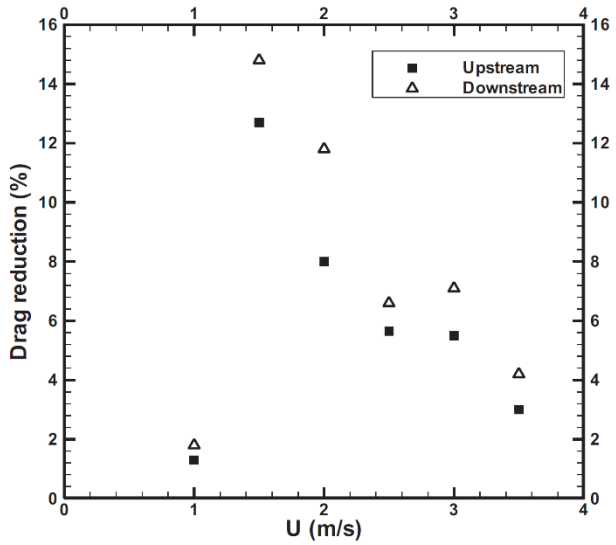

Figure 26 *Comparison of drag reduction ration with microbubbles.*

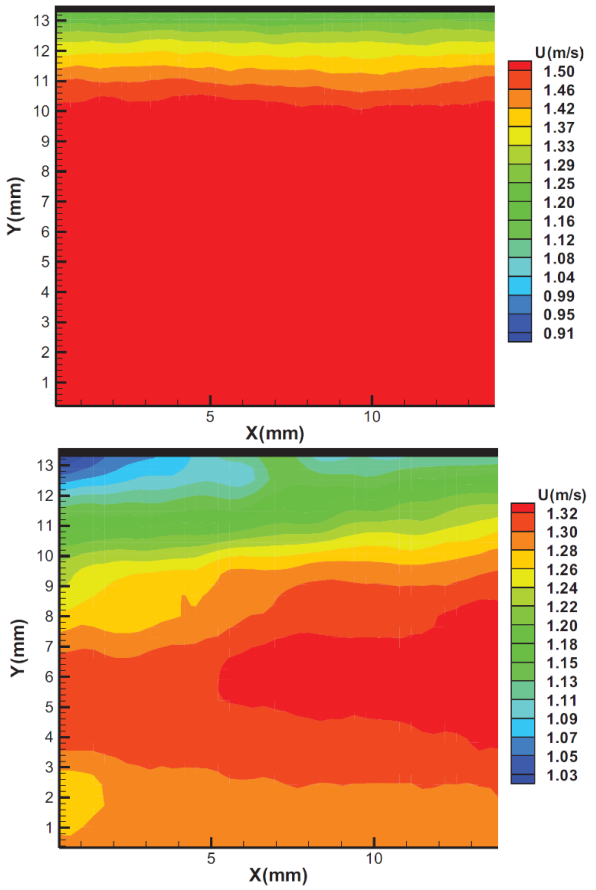

Figure 27 *Typical X-directional velocity distributions of boundary layer flows in the single (1st velocity map) and gas (2nd velocity map) phase cases at a flow speed of 1.5 [m/s]*

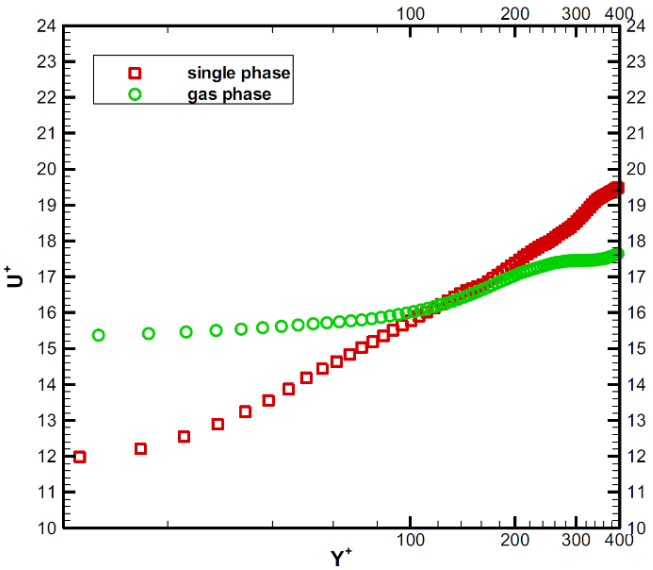

Figure 28 *Velocity profiles in the boundary layer normalized by the same single phase friction velocity at 1.5 [m/s].*

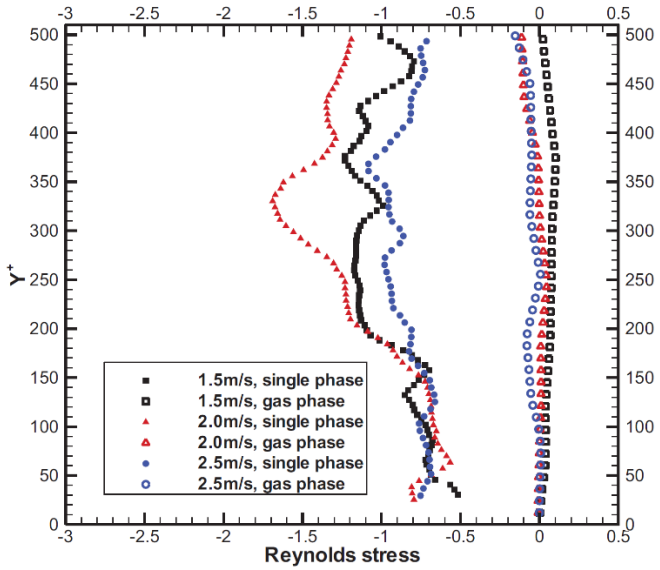

Figure 29 *Normalized Reynolds stress distributions in the single and gas phase.*

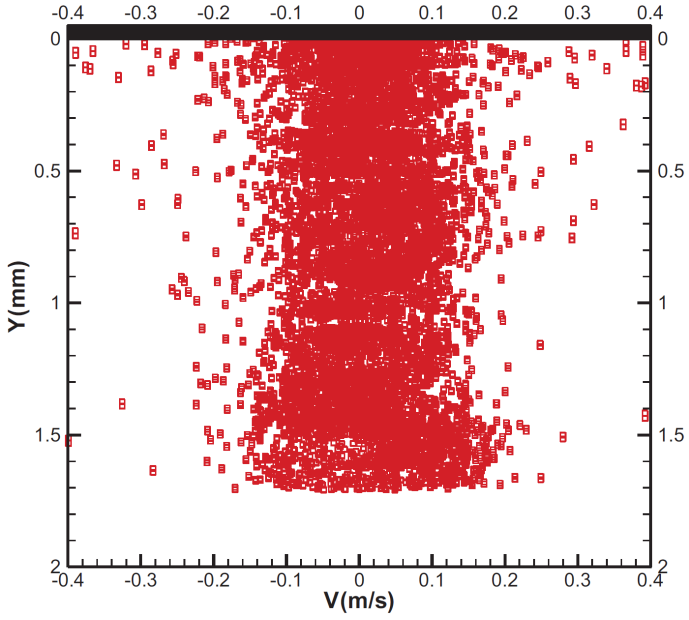

Figure 30 *Y-directional velocity (V) distribution in gas phase flows at 1.5 [m/s].*

1.4.2 Superhydrophobic Frictional Drag Reduction

The idea of superhydrophobic properties on a surface was first inspired by the unique water-repellent properties of a lotus leaf observed by Barthlott & Neinhuis 1997. The water-repellent property of the lotus leaf surface was found to be due to the microscopic morphology in forms of bumps at a scale of 10 [μm] coated by a film of wax (Rothstein, 2010). This property was also observed in many living creatures as well such as water striders where their ability to stand and move on the surface of the water was attributed to their thousands of tiny hydrophobic hair on their legs. This unique hydrophobic surface morphology inspired many researchers and scientists to mimic its surface texture in micro or nano scale and enhance the water-repellent ability.

Technically made superhydrophobic surfaces are often characterized by a rather heterogeneous and rough texture but in a micro-scale (see Fig. 31). It is worth mentioning that a difference between a hydrophobic and superhydrophobic surface lies in its micro or nano scale surface roughness and not in the surface chemistry. The air retained between the micro-peaks prevents water from wetting the whole surface and successfully keeps the water between the peaks. In other words, instead of having a single solid-water interface a transitory solid-vapor and vapor-liquid interfaces takes place.

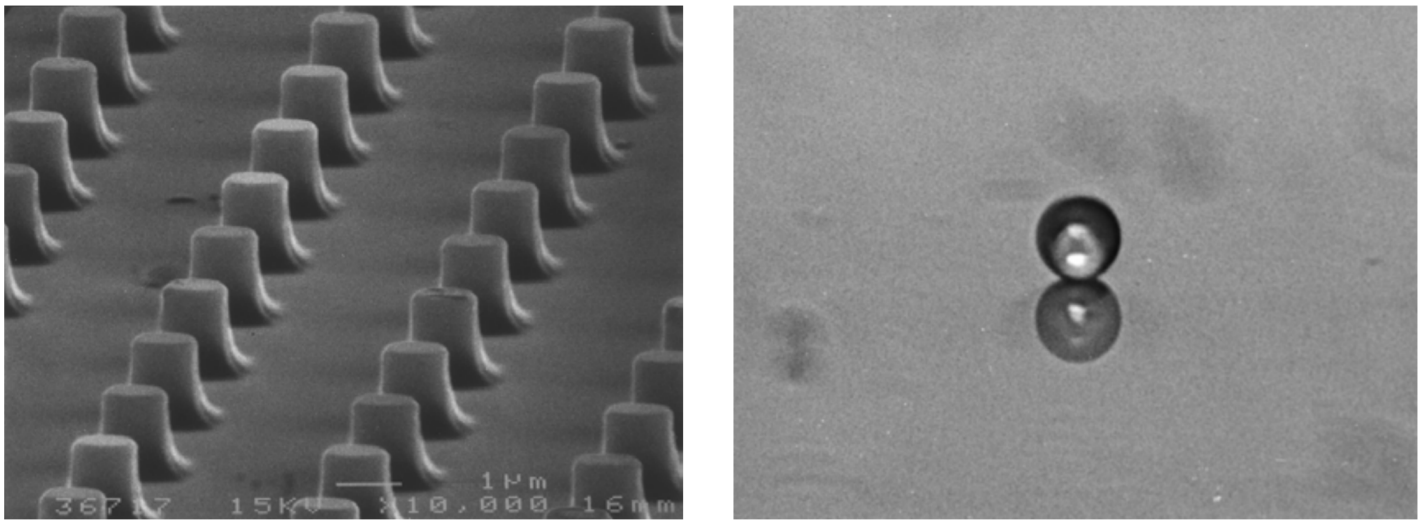

Figure 31 *Technically constructed bumps in micro scale giving a hydrophobic property to the surface.*

The first result of this micro topography is the achievement of a very large contact angle and a low contact angle hysteresis. Contact angle is the angle that a liquid droplet creates in the contact line with a solid surface (see Fig. 32). Although large amount of liquid is often affected by the gravity force in smaller droplet scales the surface forces are dominant. It was found that in hydrophobic surfaces the contact angle would increase by the surface roughness as it enhances the area where the droplet sits on a composite surface consisting of a solid and air. This can be easily confirmed in a simple experiment of dropping water on a hot fryer pan. When water drops are placed on a hot surface instead of attaching to the surface and evaporating they move almost frictionless as an air film is produced between the droplet and the hot surface avoiding the direct contact, insulating the heat, but also reducing its friction.

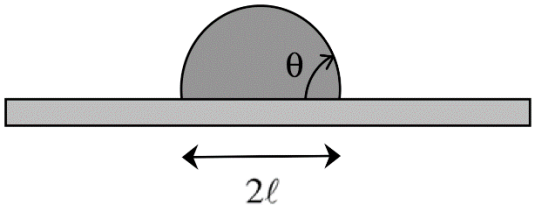

Figure 32 *Liquid droplet on a solid surface. The liquid contacts the solid surface at an angle ϑ.*

Another important consequence of this micro-morphology is the introduction of a slip boundary condition at the liquid and air-solid surface (see Fig. 33). Studies of gas flows on a superhydrophobic surface throughout the nineteenth and early twentieth century measured a slip length proving the no-slip condition to be an approximate condition. But since only few nano meters of slip were measured for macroscopic flows of simple fluids the accuracy of the no-slip condition was considered to be valid. Later on, more precise experiments at higher Reynolds number measured slip lengths ranging of 10-30 [µm] due to the air retained to the solid surface lubricating the fuild flow. Overall, the superhydrophobic surfaces were found to effectively reduce frictional drag both in laminar and turbulent flow by producing a shear-free vapor-liquid interface where the water would slip (see Fig. 34). The water depletion and air layer at the surface would further reduce the density and the viscosity of the fluid.

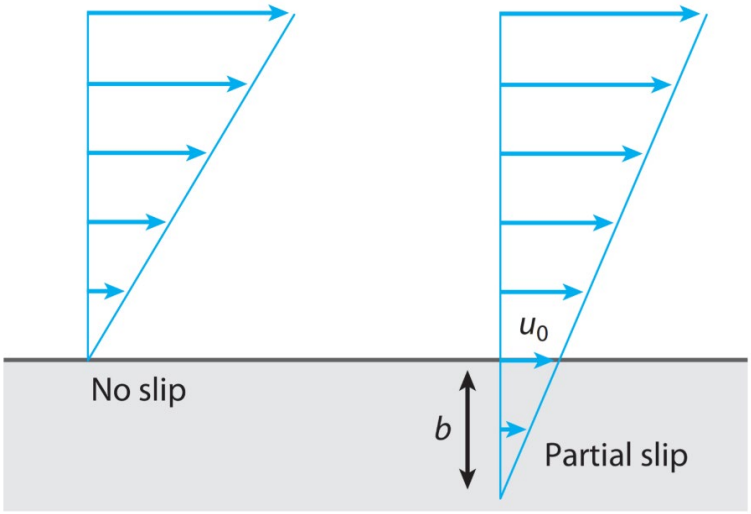

Figure 33 *No slip condition and slip condition at the liquid-surface interface.*

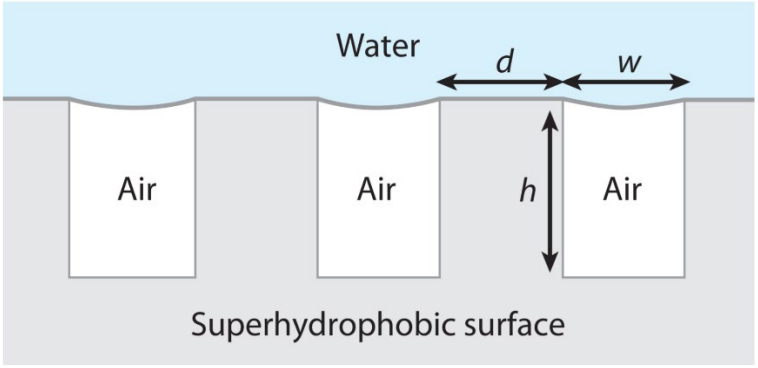

Figure 34 *Liquid-vapor interface producing a shear-free area.*

1.5 Purpose of Research & Basic Concept

The aim of this research was to experimentally examine the technique of drag reduction through the introduction of microbubbles. A careful design of the experimental work needed to be done based on the conclusions of previous studies. More specifically, as the gas volumetric flow rate appeared to be the most prevailing parameter a bubble generator with high discharge rate was necessary. Also, since the migration of bubbles away from the test area led to a decrease of drag reduction, the parallel release point of the bubbles in close proximity to the wall and a lubrication area of a flat plate seemed to be important. Last, but not least, the production of microbubbles relevant in size to the turbulent scales (diameter less than 100 [μm]), for the significant modification of turbulent structure and reduction of shear stress. For that purpose, an experimental set up with a microbubble generator attached on a ship model was proposed. An early stage of the proposal of the basic concept can be seen in Figure 35, where the experimental set up consists of a ship model with an extended flat of bottom, a microbubble generator, and external auxiliary components, such as a water pump. In this specific design the water tank attached on the inner side of the hull of the ship contains the saturated mixture of water and microbubbles while a vertical opening on the base works as a discharge point of the lubricant towards the flat of bottom. The water and atmospheric air can both be constantly supplied from the environment in order to meet the demands of the lubricant production.

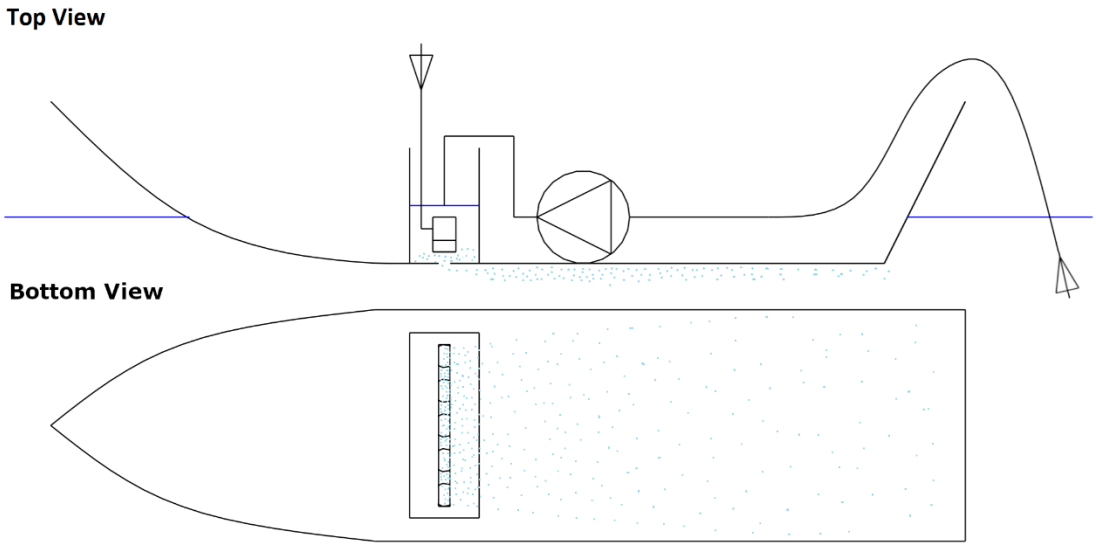

Figure 35 *Schematic view of a model ship based on the basic concept equipped with a bubble generating setup.*

MICROBUBBLE GENERATOR SETUP

In this chapter, the detailed procedures taken for the investigation of the possible experimental setup is presented first. Every viable microbubble generator is examined thoroughly and a final microbubble generator suitable for this research is chosen. The technical specifications of the final generator along with the main characteristics of the surrounding components are presented in the second section. The suggested experimental setup will provide a basic guideline for the implementation of the basic concept proposed in chapter 1.

2.1 Microbubble Generator Parameters

The generation of tiny bubbles with a diameter of fewer than 50 [μm] is a key factor in conducting this kind of experiments in precision as stated previously. As the main purpose of this experiment is the lubrication of a submerged flat surface area, the significant coverage of the available surface with microbubbles is important. For a given volume of air, microbubbles have an increased surface area that is available for the lubrication of a surface in contrast to larger bubbles. Unlike regular bubble, the microbubbles can produce a highly dense and saturated homogenous mixture of water and air for a given volume of water. Another important advantage is the buoyancy effect not acting on the microbubbles making them easier to control as they follow the flow of the liquid. Also, the great suspension time before they pop or coalescence with neighbor bubbles is another important characteristic of the microbubbles. For that matter, many viable microbubble generators (filters & diffusers) were examined as presented below.

2.1.1 “Nesia - Ns005”

Figure 36 *“Nesia - Ns005” 0.5 Micron Stainless Steel Nano-Bubble Generator.*

This generator is a stainless steel filter that can generate microbubbles through the pores of 5-50 [μm] diameter (see Fig. 36). The main advantages of this generator are the compact size of 48x12 [mm] and the extremely low cost of 3 [$/unit]. The main disadvantage is the inconsistency of the size of the bubbles. As the surface of the microbubble is produced at the hole of a pore, the bubble will continue to grow in size until the buoyancy of the air becomes greater than the surface tension. On the point of release, the bubbles are significantly bigger than the holes of each pore, making this generator unreliable for this kind of experiments that require precision and consistency. This characteristic of filters with pores has been confirmed in previous work, where the dependence of bubble size to the flow characteristics and not the pores size was confirmed (see Ch. 1). Another disadvantage of this filter is the hard maintenance of the nano-pores from internal blockages with micro dust and particles. Due to the above stated disadvantages, this filter was eliminated.

2.1.2 “Enviro Ceramic Diffuser - ECD 400”

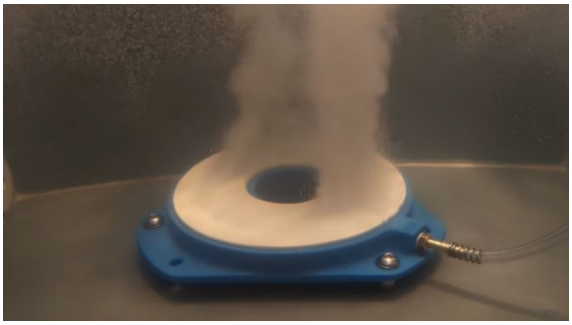

Figure 37 *“Enviro Ceramic Diffuser - ECD 400” High Pressure Ceramic Diffuser.*

The Enviro Ceramic Diffuser is a gas diffusion ceramic membrane for efficient microbubble transmission into water or other suitable liquids, made from ultra-fine nano-pores aluminium oxide (see Fig. 37). This generator produces bubbles sizes of 50-250 [µm] at 3-6 [L/min] at 100-200 [kPa]. The main disadvantages of this kind of diffuser with pores are similar to the “Ns005” filters as stated previously, which are the inconsistency of the bubble size and the high maintenance procedures for the blockage of the fine pores. This generator also has a significant size Ø292 x 40 [mm] and weight of 2.4 [kg]. Apart from the stated disadvantages, this generator was eliminated due to the complex system required for the complete installation such as a gas filter, a pressure relief valve, a flow meter and more.

2.1.3 “HOLLY - HLYZ”

Figure 38 *“HOLLY - HLYZ” High-Quality Nano Bubble Generator for Aquaculture.*

The “HOLLY – HLYZ” is a high-quality nanobubble generator for aquaculture with high efficiency and energy saving water treatment technology (see Fig. 38). The main advantage of this generator is the ability to produce nanobubbles with diameters ranging from 50 [µm] up to 200 [nm]. This generator can also produce a high saturated mixture of water and nanobubbles up to 2200 [m^3] with gas-liquid mixing proportion of 1:8-1:12. But the main reason for eliminating this generator was the high cost raising up to 6700 [$/unit] along with the unreliable size of the whole system 860 x 650 x 850 [mm].

2.1.4 "OxyDoser™ RUREair"

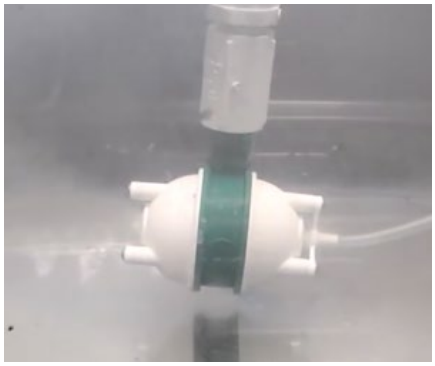

Figure 39 *"OxyDoser™ PUREair" Micro-Bubble Generator.*

The "OxyDoser™ PUREair" is a microbubble generator that can be converted from a low-pressure to a high-pressure point in order to produce variable bubble sizes while using only the power of a low wattage hydroponic water pump (see Fig. 39). This generator was available for 270 [$/unit] capable of producing microbubbles with an average diameter of 50 [µm] which is on the verge of causing unreliable bubble behaviors. Nonetheless, the ability to produce variable bubble sizes in variable pressures points, the high saturation speed along with the compact size were key advantages of this unit. While all the above specifications were satisfying the main reason of not choosing this generator was the way microbubbles are released at the discharge point, as video simulations revealed a "jet-like" discharge of the mixture. The extra power released adds an external force which leads to a fully active drag reduction technique rather than a quasi-steady energy expenditure of the microbubble drag reduction technique as stated in Chapter 1.

2.1.5 "Ylec Consultants – CARNIM D1"

Figure 40 *"Ylec Consultants – CARMIN D1" Microbubble Generator.*

The CARNIM D1 is an injector that produces fine microbubbles while requiring a simple pump generating only a few bar pressure (see Fig. 40). The main advantage of this injector is the consistent production of microbubbles, with no millimetric bubble, which maximizes the contact time and the exchange surface between the liquid and the gas while maintaining a very compact profile. The CARMIN D1 is capable of producing microbubble sizes up to 20 µm at a rate of 8 10^6 [bubbles/s] at 6 [bar] and at the cost of 655 [EURO/unit]. The disadvantage of this injector is the low flow rate at 0.018 [l/s] and the fairly high price tag. But the compact profile along with the simple required setup, able to produce consistent fine microbubble, were the main reason for choosing the CARMIN D1s to conduct the experiment.

2.2 Microbubble Generator Setup & Technical Specifications

2.2.1 Technical Specifications of "CARMIN D1"

The CARMIN D1 consists of two cylinders (upper and lower) made out of glass that is attached with two parallel screws in order to create an outlet space where the microbubbles are released with a tolerance of a 0.3 [mm] (see Fig. 41). The CARMIN D1 has two inlets: a vertical inlet where the forced filtered water by the water pump is discharged and a horizontal inlet where the atmospheric air is supplied from the atmosphere. The discharged water is further pressurized as the nozzle of the inlet tightens and the swirling motion of the water inside the CARMIN D1 creates a vacuum that sucks the atmospheric air naturally without any external mechanism. As the pressurized water and air discharges at the 0.3 [mm] space between the surfaces of the two cylinders the water and the air are mixed and a thin layer of a consistent water-microbubble mixture is released at the horizontal end point of the diameter of the cylinders. Further specifications of the CARMIN D1 are given in Figure 42 & 43 and Table 1.

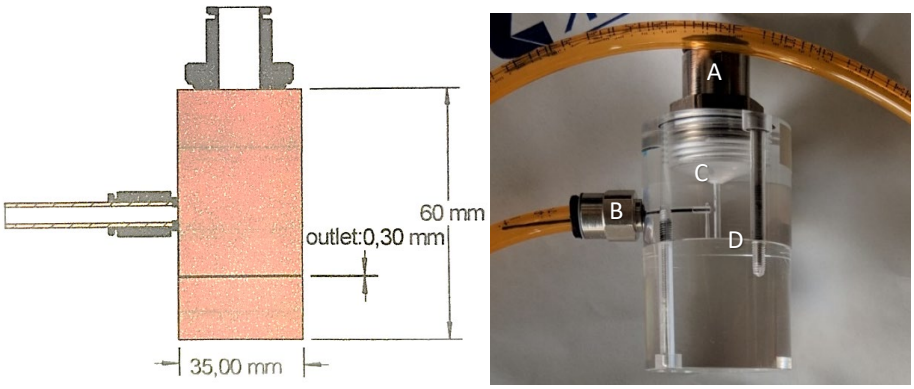

Figure 41 *Main components and dimensions of CARMIN D1 in close-up: (A) vertical inlet of water discharge, (B) horizontal inlet for air discharge, (C) conical shape for pressurization of water, (D) mixing area of pressurized water and air.*

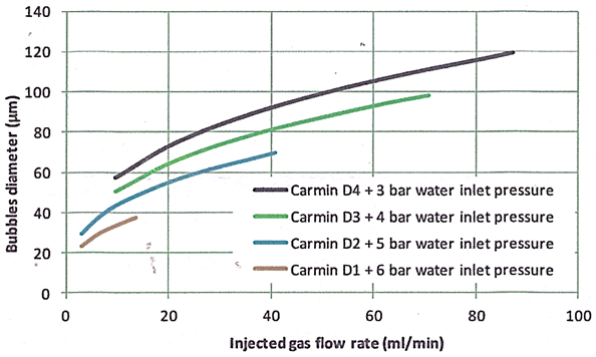

Figure 42 *Generated bubble diameter in relation to the injected gas flow rate of the CARMINs.*

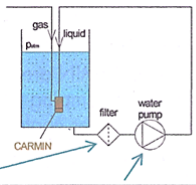

Device	Filter	Water pump	
	Water filtering (µm)	Water flow rate (l/min)	Water pressure (bar g)
CARMIN D1	75	1	6
CARMIN D2	150	4	5
CARMIN D3	225	8	4
CARMIN D4	300	13	3

Figure 43 *Characteristics of the auxiliary components: water pump and filter for the CARMINs.*

Table 1 *Specifications of the CARMINs.*

Device	Adjustable mean bubble diameter [µm]	Bubbles production rate [bubbles/s]	Water supply	
			Pressure [bar]	Flow rate [l/s]
Carmin D1	Up to 20 [µm]	$8\ 10^6$	6.0	0.018
Carmin D2	Up to 40 [µm]	$3\ 10^6$	2.0	0.050
Carmin D3	Up to 55 [µm]	$2\ 10^6$	2.0	0.100
Carmin D4	Up to 70 [µm]	$1\ 10^6$	1.5	0.180

2.2.2 Setup of “CARMIN D1”

The whole setup of the main components for the CARMIN D1s is simple and it consists of a water pump of 6 bar, a water filter, the CARMIN D1s and some plastic tubes and splitters as seen in Figure 44. Two CARMIN D1s were purchased for this set up. As presented in Figure 45 the suction line of the water pump is supplied with water while the discharge line is connected with a filter that traps any micro dirt or particles of the water, which is especially important when tap water is used instead of filtered water. The filtered water is then split into two tubes that discharge in the CARMIN D1s. The first run of this setup is presented in Figure 46 where the flow rate was tested to be 2.57 [l/min] and the capability of microbubbles generation was tested.

Figure 44 *Main components of the CARMIN D1 setup: (A) Water Pump of 6 bar, (B) plastic tubes, (C) water filter, (D) 1-2 splitter tube, and (E) CARMIN D1 [x2].*

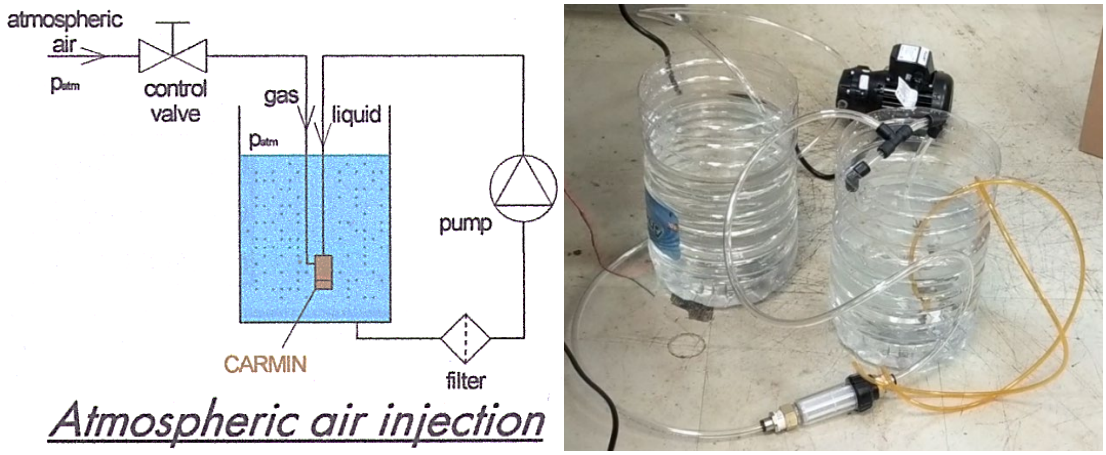

Figure 45 *A schematic view of the device arrangement for the microbubble generation (left side) and an actual setup of the whole setup for the CARMIN D1s (right side).*

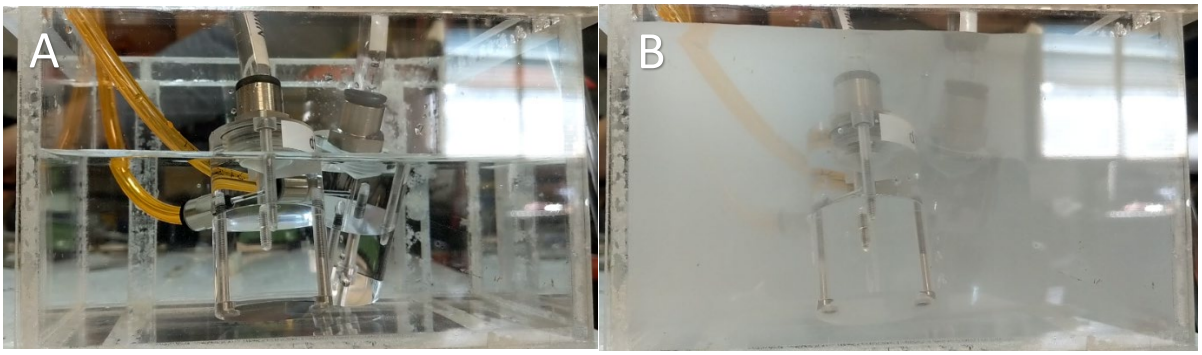

Figure 46 *Microbubble Generation of the CARMIN D1s: (A) unsaturated clear water (water pump: off), (B) fully saturated water with fine microbubbles (water pump: on).*

In this chapter, all the procedures taken in order to conduct the experiments are presented in detail. In the first section, the implementation of the basic concept in a downscaled experiment is presented along with proposals for improvements in the design based on critical observations. In the second section, the upscaled implementation of the basic concept is presented based on previous results. In the last part, all the procedures of the measurements and testing conditions are presented.

3.1 Implementation of the Basic Concept

3.1.1 Downscaled Version

Before the full-scale implementation of the basic concept introduced in Chapter 1, a downscaled experiment was conducted on a small sized water tank (5.0 x 1.5 x 1.5 m) in the Laboratory of Naval and Marine Hydrodynamics at NTUA. The testing in a downscaled experimental version were necessary to be conducted, in order to investigate the suggested setup of the CARMIN D1s, the optimum method of microbubble generation utilization, and the behavior of the microbubble flow in macro scale. It is necessary to be stated, that no measurements were conducted and only visual observations were taken into account at this first stage. For that purpose a downscaled box-like shaped ship was made out of plastic foam with the dimensions L = 1200, B = 200, D = 150 [mm] (see Fig. 47). The flat of bottom was constructed out of two pieces of flat plates made out of glass, as the observation of the flow characteristics of the microbubbles was crucial at this early stage of testing. The ship model was watertight throughout its length while the stem area had a vertical opening for the discharge of the mixture of water and microbubble only through the act of gravitational force.

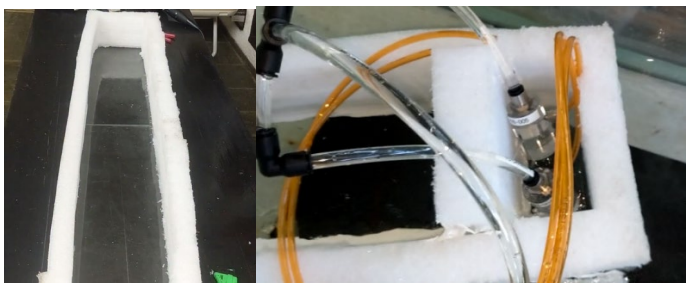

Figure 47 *Downscaled version of the basic concept: "Box-like" ship model from a top view (left side), installation of CARMIN D1s at the non-watertight stem side (right side).*

For each run, the ship was towed in one direction, while the pump was working in a non-wetted area, in order for the CARMIN D1s to produce microbubbles at constant rate at the stem area. During each run, a flashlight was projected into the direction of the microbubbles and a black tape was installed at the bottom of the water tank in order to increase the contrast of the bubbly flow and better observe their behavior (see Fig. 48). Through the visible flat of bottom an even lubrication throughout the whole extent of the width was noted, indicating a sufficient production of microbubbles. The microbubbles were characterized by a rather high suspension time, unaffected by the effect of buoyancy or coalescence, as a diffusion in all direction was noted even in the leftover microbubbles at each run. After each run, the flat of bottom was examined and the whole flat of bottom was found to be fully covered with microbubbles attached on it, leading to the qualitative conclusion that the microbubbles were acting within the boundary layer (see Fig. 49).

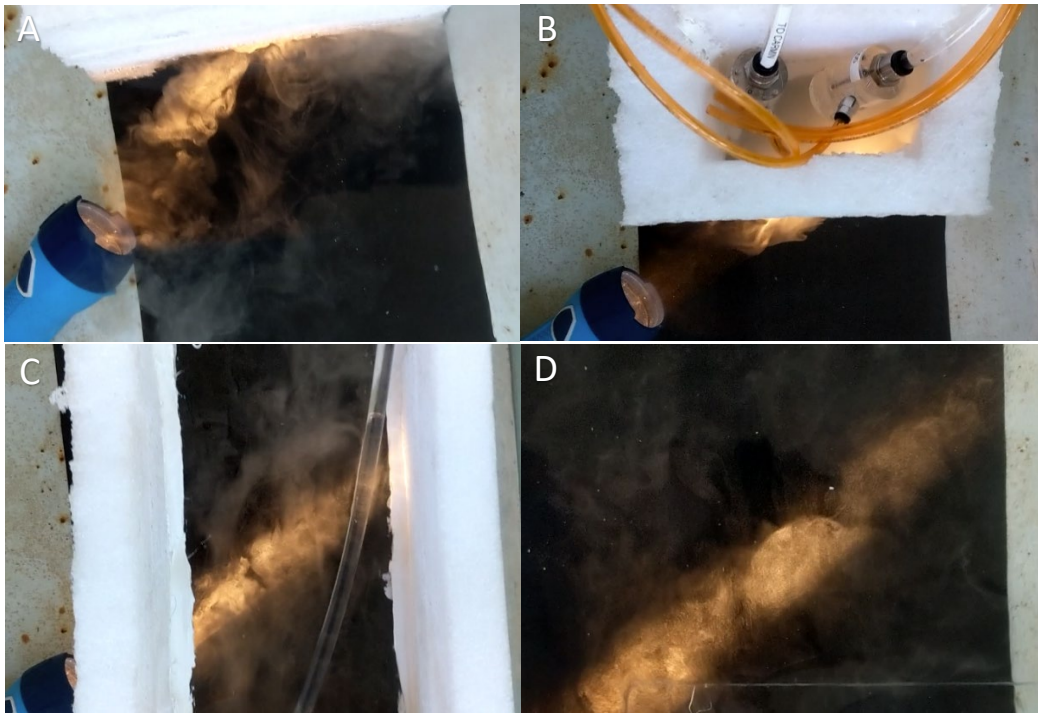

Figure 48 *Implementation of the basic concept: (A) Diffused generated microbubbles in front of the stem area, (B) Generation of microbubbles at the non-watertight stem area, (C) Lubrication at the half-length area with microbubbles, (D) Leftover microbubble after the run.*

Figure 49 *Visible microbubbles through the glass flat of bottom attached on the surface after each run (Top view).*

Based on the above implementation, few downsides were noted as well. The vertical release point seemed to be not the optimal as the vertical discharge along with the gravitational forcing acting upon the mixture appeared to diffuse the microbubbles in all directions, minimizing the effect of microbubbles interaction with the flow in the direction parallel to the flat plate (see Fig. 50). The direction of the discharge point is crucial, since the microbubbles unaffected by the effect of buoyancy are prone any force acting on them and as a result lead them off-track and migrate them away from the horizontal direction. It is worth noting that as the resultant velocity is the equivalent to the combined velocity of gravitational velocity and free flow velocity, this effect can be minimized further in higher towing speeds.

Figure 50 *Diffusion of the generated microbubbles in all directions at the discharge point of the stem area.*

In order to upscale this implementation into a full-scale ship model, the saturation ability of the two CARMIN D1s was tested in a 10 [L] of a water. The two generators were sufficiently enough to lubricate a surface area of the "box-like" ship model which as approximately 0.24 [m^2], but their coverability on a bigger surface area needed to be confirmed. During the test the two generators were at constant rate releasing microbubbles, and after 5 [min] the mixture reached its maximum saturated condition, possibly due to the effect of coalescence or because of reaching its maximum suspension time, which was far from being fully saturated (see Fig. 51). As a result, further optimization of the basic concept needed to done.

Figure 51 *Saturation test of the two CARMIN D1s: In 5 minutes the mixture reached its pick of saturation and no further saturation was noticed.*

3.1.2 Improved Concept

Critical improvements in the design of the basic concept was necessary to be conducted based on the stated above conclusions. More specifically, void fraction in the horizontal direction needed to be optimized through an optimized the discharge point, while dealing with the low saturation rate of the two generators. As a natural consequence, the idea of installing the two CARMIN D1s directly at the stem area of the flat of bottom was proposed as an improved concept. With this approach every single microbubble generated is discharged horizontally without any gravitational force leading to migration and lead to a direct attachment on the testing surface area. Also, the saturation ability of the generators are optimally utilized as every single microbubble produced is utilized while no "dead-time" is given for the coalescence to act. A preview of the improved concept is seen below, Figure 52.

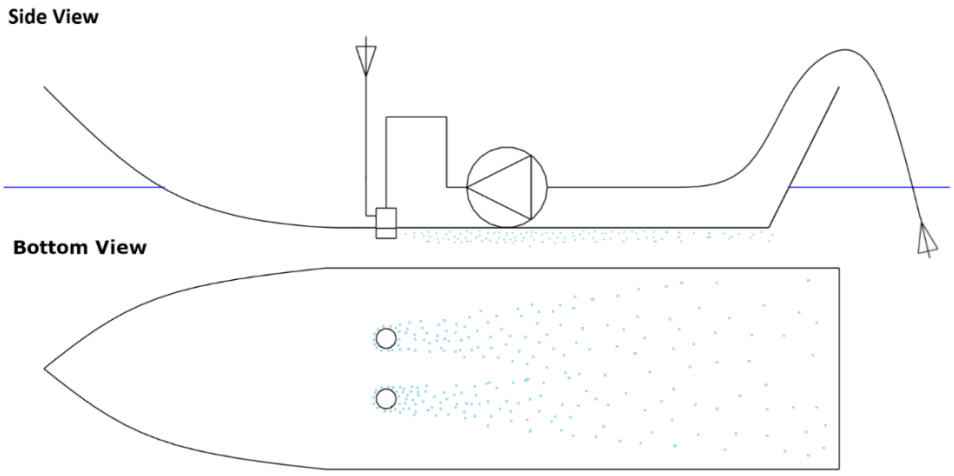

Figure 52 *Schematic representation of the improved concept: CARMIN D1s installed directly at the flat of bottom.*

3.2 Implementation of the Improved Concept

3.2.1 Upscaled Version

In this stage, a full-scale experiment for more precise measurements and observations was conducted in the Towing Tank of the Laboratory, which is 100 [m] long and 4.6 [m] wide. The aim of the full-scale experiment was to examine the effect of microbubbles' introduction in the boundary layer of a ship model. For that purpose, a ship model with specific design characteristics, such as extended flat of bottom, needed to be constructed in order to meet the needs of this experiment. The experimental design was simplified as much as possible in order to eliminate as many external parameters as possible and examine only the effect of frictional drag in the presence and absence of microbubbles.

3.2.2 Ship Model Dimensions

In the first stage, the basic dimensions of the ship model were calculated. Considering the average drag reduction found in similar studies, 3-5%, the minimum drag reduction was chosen as a first reference of our calculations. Also, due to the limited measurement accuracy of the dynamometer of the towing tank and the presence of external frictional vibrations on the towing rails, the minimum measurable difference $\Delta F = F_{No\ Microbubbles} - F_{With\ Microbubbles}$ was set to be at least greater than 5 [g]. A measured difference in drag less than 5 [g] would allow external forces due to vibrations to be the primary factor while maximizing the uncertainty of the results. In order to determine the dimensions of the ship model, possible combinations of L and B and the corresponding drag difference were calculated through a repeated process. The towing speed was set to u = 1.5 [m/s], the density of water at $\rho = 997$ [kg/m^3], and viscosity of water at $\nu_{18\ oC} = 1.0533\ 10^{-6}$ [m^2/s]. L = 2.5 [m] and B = 0.5 [m] provided a reasonable dimension ratios and a total measured drag difference above the minimum measurement accuracy. Frictional drag of the ship model was approximately calculated as the frictional drag of a flat plate. It is also worth noting that since this approximation was based on a simplified structure of a flat plate, the residuary drag forces due to the complexity of the structure of an actual ship model along with the higher towing speed will ensure measured drag difference above the minimum measurement accuracy.

The frictional drag of a flat plate is given by the following equation:

$$F = \tfrac{1}{2}\, \rho\, u^2\, L\, B\, C_d \qquad \text{(Eq. 1)},$$

whereas the Reynolds number is given as:

$$Re = u\, L / \nu \qquad \text{(Eq. 2)},$$

and the friction coefficient for turbulent flow:

$$C_d = 0.074 / Re^{1/5} \qquad \text{(Eq. 3)}.$$

3.2.3 Ship Model Construction

Based on the above calculated dimensions a ship model was constructed out of plywood at the carpentry of the Laboratory (see Table 2, Fig. 53 & 54). The unique design aspect of this ship model is the extended flat of bottom throughout its length, the pointed bow, and the low draft in order to minimize residuary drag forces, such as the wave-making and wind resistance and maximize the frictional drag as the primary force acting on the ship. Apart from the main characteristics, further important structural details are presented below. First and foremost, longitudinal girders were attached at the end of each side almost along the entire length of the ship, in order to prevent microbubbles' escape from the flat of bottom to water surface through ship's both sides and as a result improve air retention (see Fig. 55).

Table 2 *Main dimensions of the ship model*

Main Dimensions	
L [m]	**2.52**
B [m]	**0.50**
D [m]	**0.15**

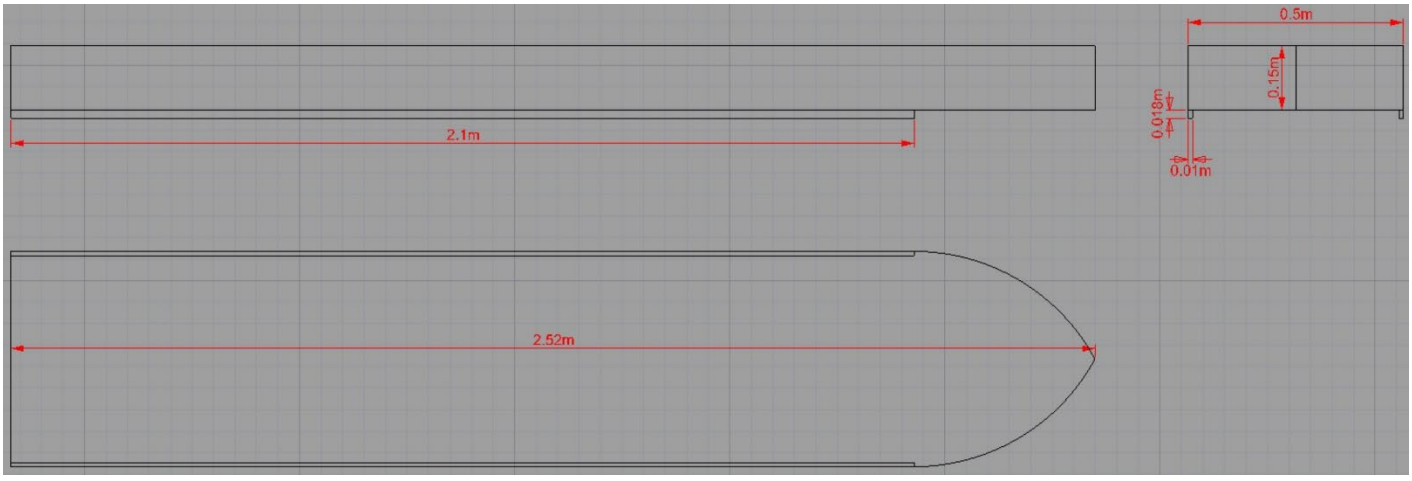

Figure 53 *Main dimension of the ship model in Rhino 3D.*

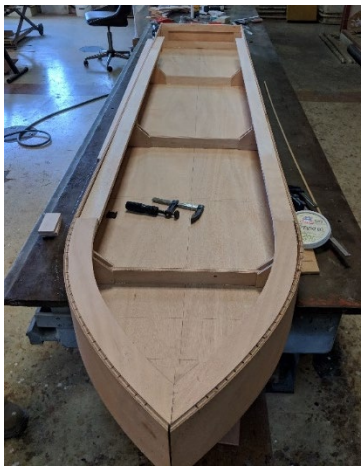

Figure 54 *Constructed ship model at the carpentry of the Laboratory.*

Figure 44 *Longitudinal girders along the end of each side for air retention.*

Another important structural detail are the two custom openings in order for the CARMIN D1s to be extended from the flat of bottom (See Fig. 56). In order to ensure that the CARMIN D1s are hold in place and watertight two custom holders were patented (See Fig. 57). A final view of the installation of the CARMIN D1s is shown in the Figure 58. The two CARMIN D1s were extended as much as the each outlet was leveled with the plane surface of the flat of bottom, in order to encourage the microbubbles to be diffused horizontally on the surface area. At the end, the surface was coated with a conventional painting.

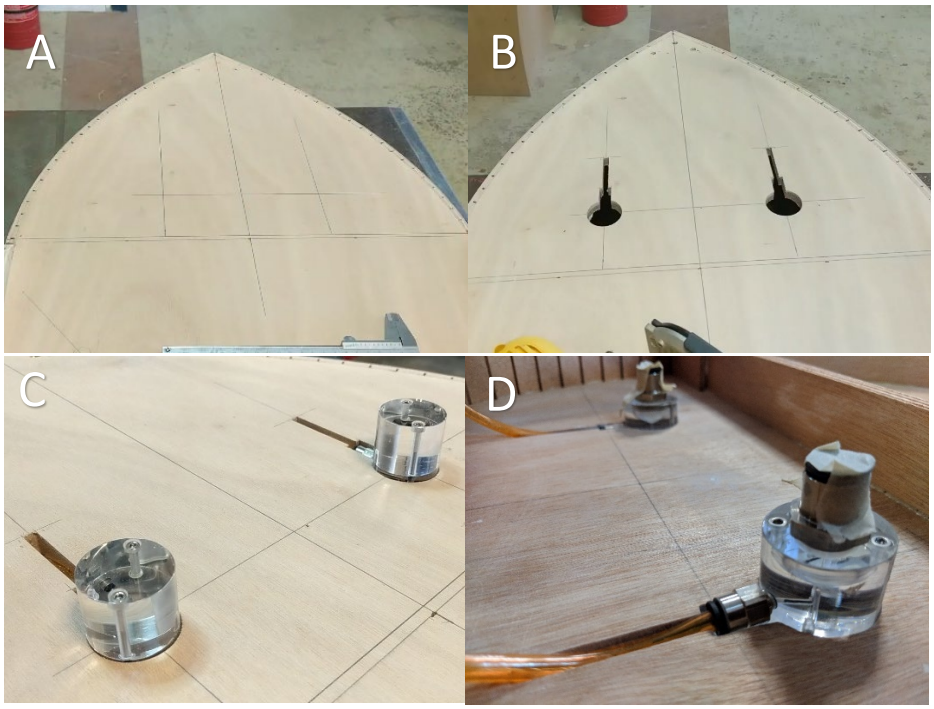

Figure 56 *Custom openings on the flat of bottom: (A) Stem before the opening (bottom view), (B) Stem with the two custom openings (bottom view), (C) The two CARMIN D1s fitted at the openings (bottom view), (D) The two CARMIN D1s fitted at the openings (top view).*

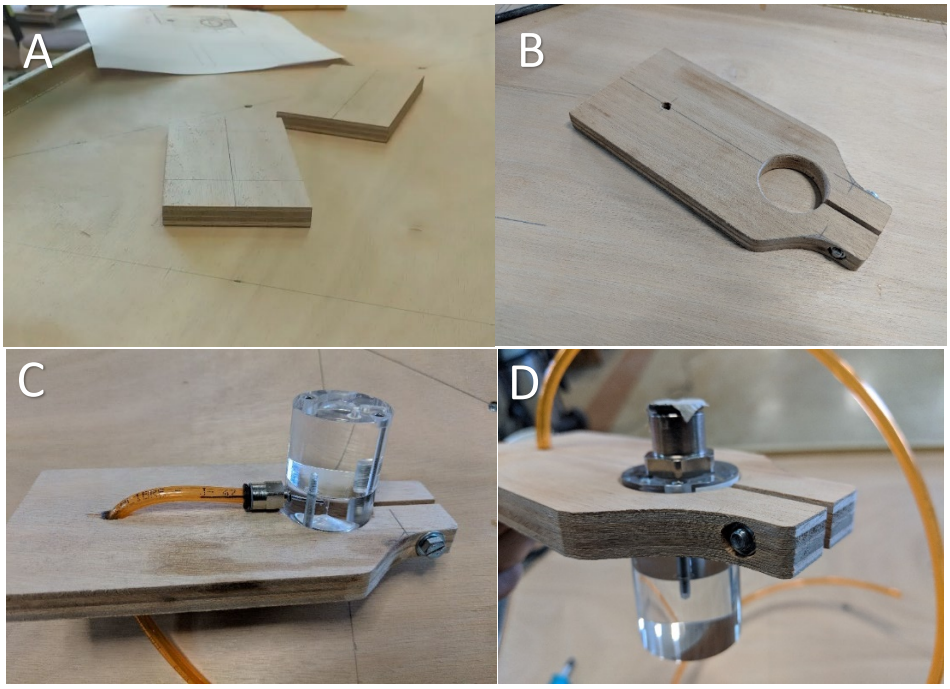

Figure 57 *Custom holders for the CARMIN D1s: (A) Two blocks of MDF, (B) MDF's circular opening modified for the insertion of the CARMIN D1s' cylinder, (C) CARMIN D1 fitted (bottom view), (D) CARMIN D1 fitted (top view).*

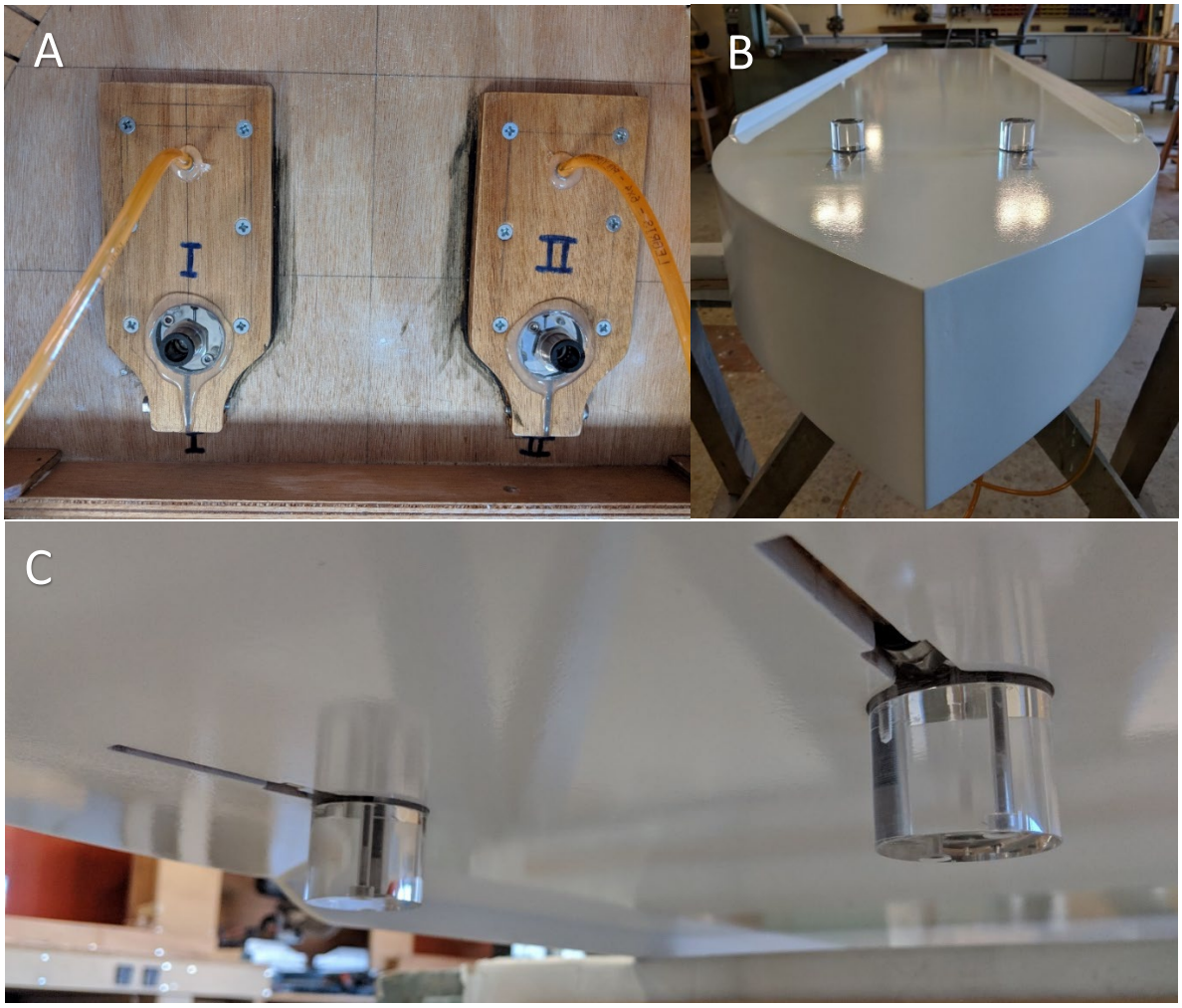

Figure 58 *Final installation: (A) CARMIN D1s attached (top view), (B) CARMIN D1s extended from the flat of bottom (bottom view), (C) Outlet of the CARMIN D1s leveled with the horizontal plane (bottom view).*

After the final construction, the whole set up was tested in the towing tank at a stationary condition. Video obervations over the surface and underwater confirmed that the bubbles diffused in a parallel direction due to the leveling of discharge outlet of the CARMIN D1s with the horizontal plane (see Fig 59).

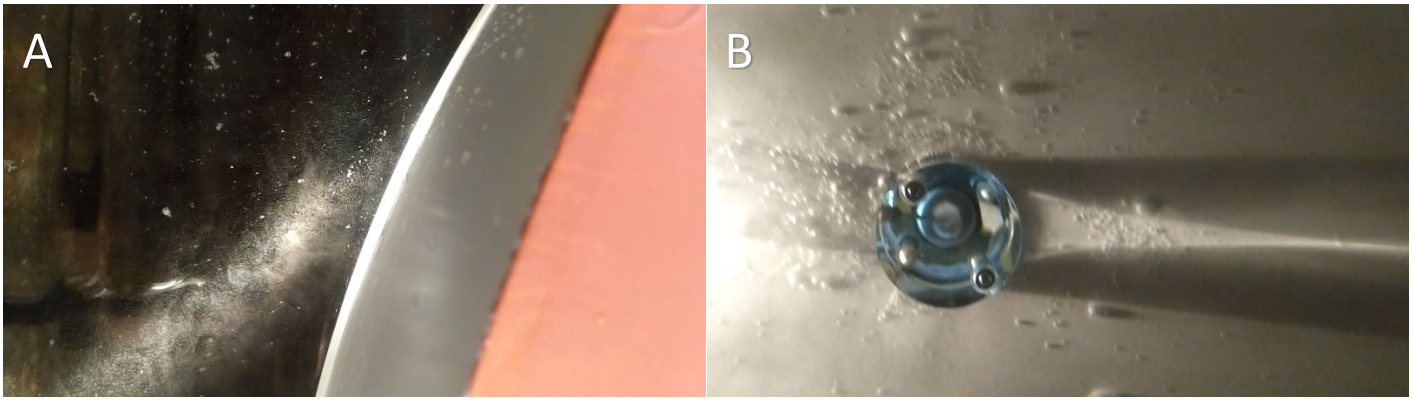

Figure 59 *Video observation of the discharged microbubbles: (A) Fog of microbubbles diffusing horizontally at the stem area (top view), (B) Fog of microbubbles diffusing horizontally on the flat of bottom (bottom view).*

3.2.4 Optimization: 1st Phase

Series of towing experiments were conducted after the final construction of the ship model. Details of the experimental procedures and results are presented in the last part and next chapter. After the conduction of the first experiments few optimizations were made in order gain more drag reduction. First, the outlet of the CARMIND D1s were optimized so that the tolerance might be at the exact level with the plane surface of the flat of bottom. As it can be seen in Figure 60, before this optimization the outlet of the generators and the level of the flat of bottom had a height difference of 1.5 [mm] that was later on optimized to almost 0.0 [mm]. With that a better directed ejection was aimed in order to introduce the microbubbles directly to the surface area and boundary layer. Secondly, a turbulence stimulators was fitted to the ship model forward to the generators, 5% of the model's length aft the bow, in order to increase the boundary layer (see Fig. 61). Turbulence stimulator's diameter was chosen accordantly to the ITTC standards provided by a specific program of the laboratory, where the temperature and density of the water were inserted. Turbulence stimulator was added in order to compensate the violation of Reynolds similarity and enforce laminar-turbulent transition in the model roughly at the same location as in full scale. But more importantly, the further stabilization of the boundary layer was attempted in order to retain as many microbubbles and minimize the effect of migration away from the near surface. Lastly, the dynamometer's locking base on the ship model was altered to 1^{o} angle so that the ship may trip by the stern (see Fig. 62). This modification was proposed in order to increase the persistence of the microbubbles further downstream, as the relaxation of the flow to its original state due to the re-establishment of high shear on the surface was leading to major decrease in frictional drag reduction.

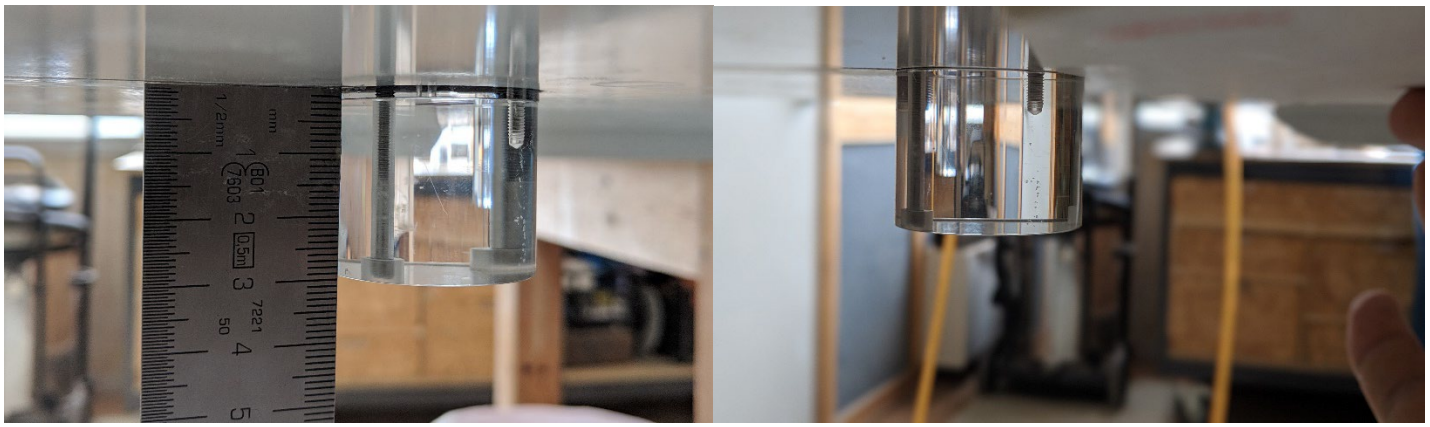

Figure 60 *Optimization of CARMIN D1 outlet's position: a) Before the optimization (left side), b) After the optimization (right side).*

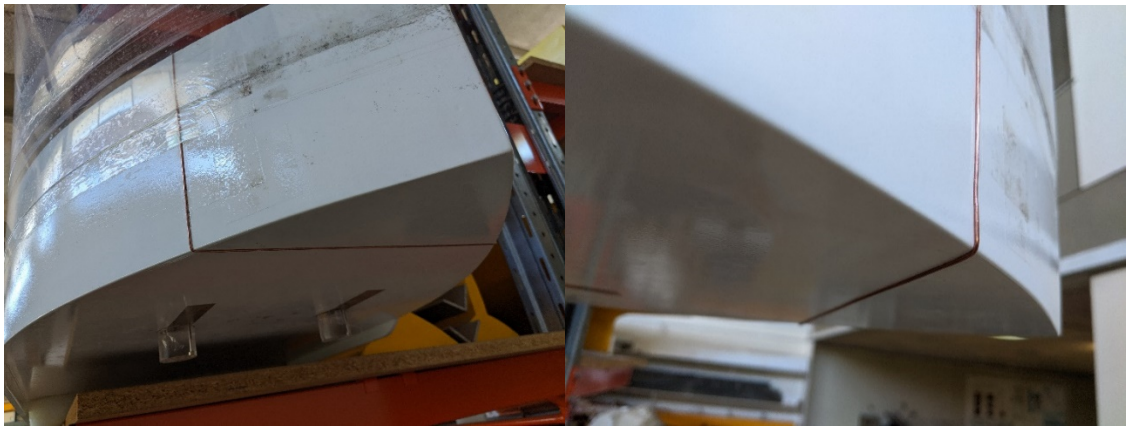

Figure 61 *Turbulence stimulator fitted at the bow area, 5% of the total length.*

Figure 62 *Modification of the locking base of the dynamometer by altering to 1º of trim by the stern.*

3.2.5 Optimization: 2nd Phase

At this last stage, a final attempt to further increase drag reduction was done by altering the surface painting material. As it was mentioned before, the ship model was painted with a conventional paint. In order to increase microbubble's attachment to the surface and overall interaction a super hydrophobic coating was applied in the laboratory of "Ceramic Pro" (see Fig. 63). Based on similar works presented in the Literature Review, the increase of the surface tension through the application of a super water repellent coating and consequently maximization of the frictional drag reduction was aimed.

Figure 63 *Superhydrophobic coating "Ceramic Pro" applied on the flat of bottom.*

3.3 Experimental Procedures

The drag resistance measurements were conducted in the towing tank of the laboratory of Naval and Marine Hydrodynamics at NTUA. During each set of experimental measurements a precise and repetitive procedures were carefully conducted. Typical steps of the procedure involved in each series of experiments are presented below.

First, the temperature of the fresh water of the tank was measured each day and recorded for each test series. During the 4 months period the water temperature ranged from 13.3 to 20.3 [^{o}C]. The recording of the water temperature was crucial in order to calculate the unique density of each day. Also the temperatures were recorded for the conversion of all measurements into same testing condition using as a reference the nominal temperature of 15 [^{o}C]. Before the first run, the dynamometer was calibrated using a series of masses ranging from 0.25 to 2.05 [kg]. Calibration points with big deviation from the linear fit were excluded as measurement errors. Calibration of the dynamometer was used in order to convert the output voltage of the dynamometer to kiloponds, in other words convert the electrical signals to force units through the calculation of the linear transfer function. After the calibration, the ship model was attached to the resistance dynamometer via a fitting plate located longitudinally at the corresponding longitudinal center of gravity and transversely at the center line. As for the setup, only the CARMIN D1s along with the tubes for the suction of the filtered water and atmospheric air were attached on the ship model, while the rest of the auxiliary components such as the pump, the filter, and the water bucket were placed on the towing carriage (see Fig. 64). As it can be seen, the bow area was covered with a plastic sheet in order to prevent water wetting the inner side.

For each run, the average model's resistance, the dynamic trim and heave, and the towing speed were sampled simultaneously from the dynamometer's output which were automatically saved in a .txt format. Between each run an interval of 15-20 [min] was given in order to conduct its measurement in the same calm water condition. Also before each run the residual outputs of the system at quiescent condition were calculated in order to deduct the minimum outputs from the final measurements and record the remaining real friction each time. The dynamometer was connected to a graphics card of the towing carriage which collected the data at a rate of 100 [Hz] for variable lengths of time depending on the towing speed. The sensitivity of the card was further increased for more accurate measurements especially at lower speeds. The ship was tested at various speeds, with and without the microbubble generation, on a conventional painting and superhydrophobic coating, at even keel and trim by stern, all the results and the analysis of which can be found in the next chapter. The details of the conducted test series along with the experimental conditions are presented in the Table 2 below. In Figures 56 & 66 the wave making of the ship model and microbubble lubrication at the flat of bottom at various towing speeds can be seen.

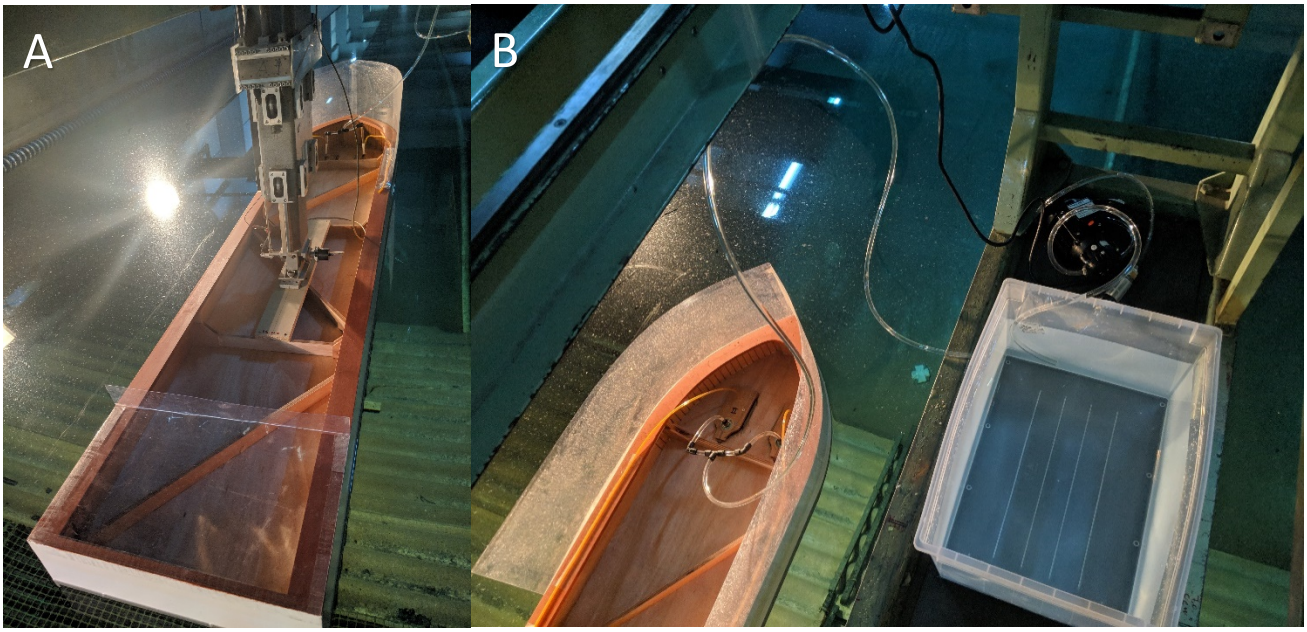

Figure 64 *(A) Installation of the ship model at the dynamometer of the towing tank, (B) Setup for the CARMIN D1s.*

Table 2 *All testing conditions*

Testing Conditions		Speed [m/s]	# measurements
Even Keel	*Modification: 1st Phase*	0.5	5
		1.0	3
		1.5	26
		2.0	12
Even Keel	*Modification: 2nd Phase*	1.5	10
		2.0	10
		2.5	10
Trim by Stern 0.5º	*Modification: 1st Phase*	0.1	8
		1.5	8
Trim by Stern 0.5º	*Modification: 2nd Phase*	1.0	2
		1.5	12
		2.0	22
		2.5	20

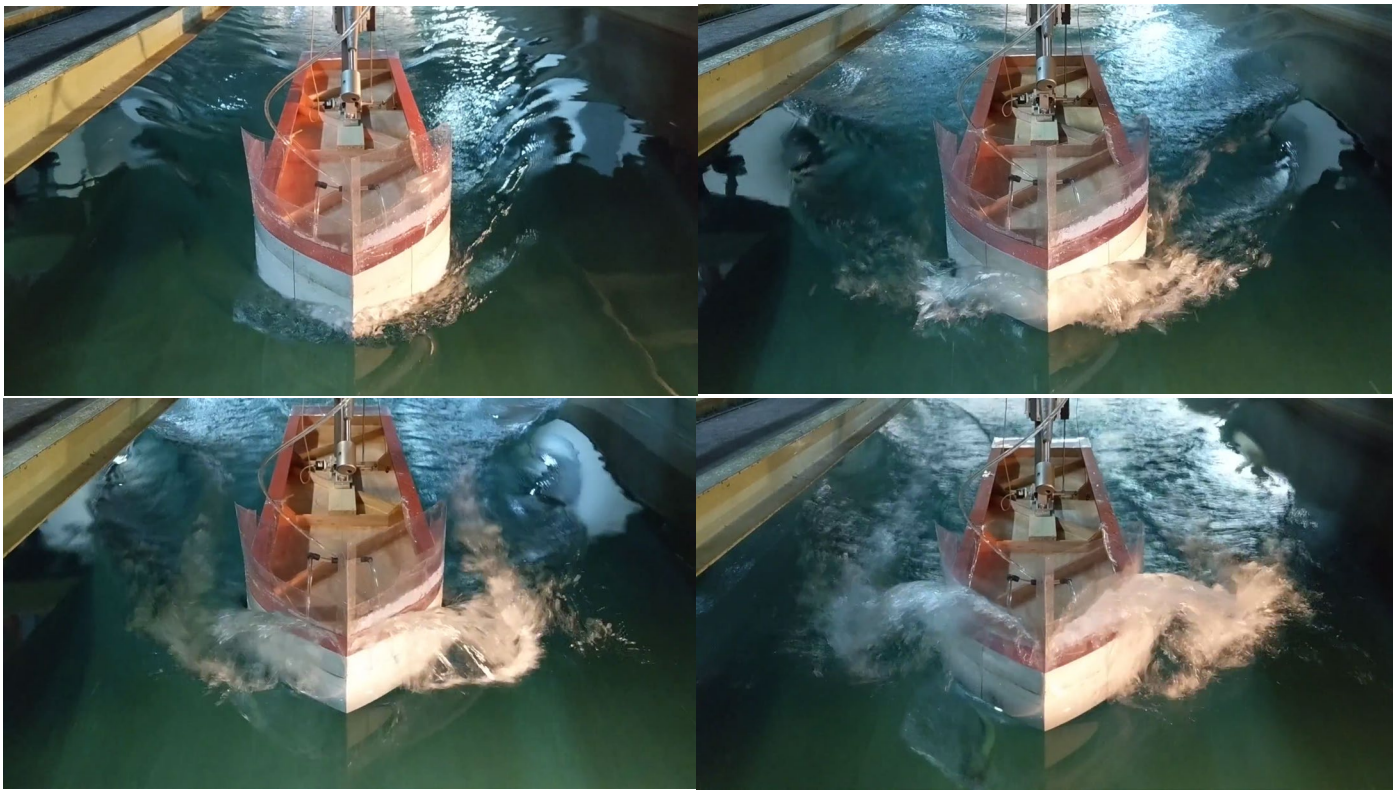

Figure 65 *Drag measurements at even keel for various towing speeds: a) V = 1.0 [m/s] (top left), b) V = 1.5 [m/s] (top right), c) V = 2.0 [m/s] (bottom left), d) V = 2.5 [m/s] (bottom right).*

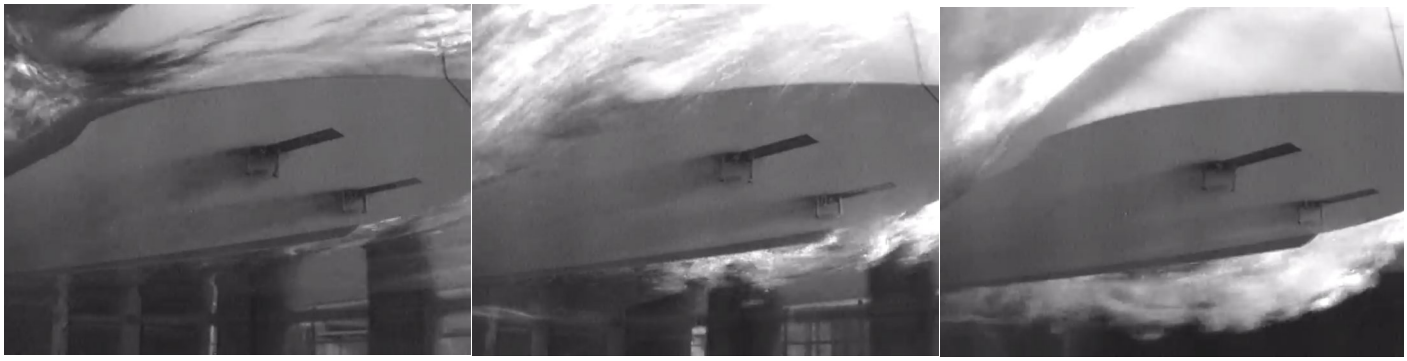

Figure 66 *Video observation of microbubble lubrication during various towing speeds at even keel: a) V = 1.0 [m/s] (left), b) V = 1.5 [m/s] (middle), c) V = 2.0 [m/s] (right).*

EXPERIMENTAL RESULTS & ANALYSIS

In this chapter, the experimental results are presented in detail. In the first section, the procedures followed for the calculations of the experimental measurements are presented analytically. In the second section, an evaluation of the measurements is conducted in order to confirm the validity of the experimental results. In the third and last section, the final experimental results are presented and the effect of the microbubbles in the reduction of frictional drag is interpreted studies.

4.1 Experimental Results Processing and Calculations

A precise procedure was followed for the numerical calculation of the resistance experimental results. First and foremost, the residual voltage output was recorded before each run as V_0 and during each run the average measured voltage of the dynamometer was recorded as V_{towing}. The remaining voltage is equal to the real voltage solidly due to the ship model resistance alone, $V_{real} = V_{towing} – V_0$. In order to change the electrical signal of the dynamometer into force units the remaining voltage was multiplied by the slope "a" of the linear transfer function, y [kp] = a x [V] + b, in order to obtain the total resistance R_T [kp] = a ΔV = a V_{real}. For practical reasons it was further converted into Newton units by being multiplied by 9.81, since 1 [kp] ~= 9.80665 [N].

In order to calculate the skin friction coefficient of the measurements without microbubbles $\underline{C_{F\ w/o\ bubbles}}$ (referred as C_F from now on) the following method was followed. The R_T was estimated to be a sum of two components: the frictional resistance R_F and the wave-making resistance R_W which also includes all the remaining aggregated residual resistances, such as wind resistance (see Eq. 4). The frictional resistance was calculated using an approximate method (see Eq. 5), were ρ [kg/m^3] is the density of water at a specific water temperature, U [m/s] the average towing speed, and S [m^2] the wetted surface of the ship model. The frictional coefficient C_F can be calculated according to the ITTC-1957 frictional correlation line (see Eq. 6). Reynolds number was calculated using the following Eq. 7 where ν [m^2/s] is the kinematic viscosity of the water at a specific water temperature. It is worth noting that this method has some computational errors as it is assumed that the ship model has a perfect flat plate while ignoring the construction detail of the bow and the extended two CARMIN D1s in the form of cylinders interrupting the free flow. In other words, the estimated skin friction coefficient or the frictional drag of the ship model is less than the real value.

$$R_T = R_F + R_W \quad \text{(Eq. 4)}$$

$$R_F = ½\ \rho\ U^2\ S\ C_F \quad \text{(Eq. 5)}$$

$$C_F = 0.075 / (\log_{10}Re – 2)^2 \quad \text{(Eq. 6)}$$

$$Re = U\ L / \nu \quad \text{(Eq. 7)}$$

In order to calculate the skin friction coefficient of the measurements with microbubbles $C_{F\_w/\ bubbles}$ (referred as $C_{F'}$ from now on) the following method was followed. The same estimation for the $R_{T'}$ and its components was used (see Eq. 8) but this time $R_{F'}$ was not measured through the ITTC-1957's proposed method as this method does not assume the presence of microbubbles interacting with the boundary layer and altering the structure of the turbulent flow. Instead it was estimated that the residual resistance remained the same regardless of the presence or not of microbubbles, $R_W = R_{W'}$. This assumption can be considered as the microbubbles which are free of buoyancy effect cannot affect the dynamic heave or trim of the ship model during the towing and consequently alter the wave-making resistance. Pitch and heave representation plotted against the sequence of measurements altering between the conventional resistance measurement and resistance measurement with the presence of microbubbles, portray a rather steady and consistence results regardless of the presence or absence of microbbubles (see Fig. 67-82). Also it should be mentioned that regardless of the introduction or not of microbubbles the towing carriage ran at the same speed during each test series indicating that the wave-making resistance which is proportional to its speed value remained the same. Having the $R_{T'}$ and $R_{W'}$ the frictional resistance $R_{F'}$ can be calculated and consequently the skin friction coefficient $C_{F'}$ (see Eq. 9). It is worth noting that due to the previous conventional calculation of the ITTC-1957 method not estimating the presence of the two generators, a computational error is carried throughout this rest of the calculation process. More specifically, due of C_F's underestimation, R_F is underestimated accordingly, leading to a slight overestimation of R_W. But since $R_W = R_{W'}$ the net difference of the skin friction resistance with and without microbubbles is not affected (see Eq. 10) while the computational error is carried throughout the reduction rate of the frictional resistance (see Eq. 11). In other words, the rate of frictional drag reduction, $\%r_{RF}$, will always be a slightly overvalued due to the presence of R_F as the denominator in Eq. 11.

$$R_{T'} = R_{F'} + R_{W'} \qquad \text{(Eq. 8)}$$

$$R_{F'} = ½\ \rho\ U^2\ S\ C_{F'} \qquad \text{(Eq. 9)}$$

$$\Delta R_F = R_F - R_{F'} = (R_T - R_W) - (R_{T'} - R_{W'}) = R_T - R_{T'} \qquad \text{(Eq. 10)}$$

$$\%r_{RF} = (R_{F'} - R_F) / R_F = (R_T - R_{T'}) / R_F \qquad \text{(Eq. 11)}$$

Finally, all the above values conducted at different water temperatures were converted into the nominal temperature of 15 [^oC] based on the "Recommended Procedures of ITTC 7.5-02-02-02" (see Eq 12), where C_T is the total resistance coefficient, and 1+k the form factor. In order to define the form factor the method mentioned in the "Recommended Procedures of ITTC 7.5-02-02-01" was followed based on the Prohaska method. The form factor can only be experimentally evaluated and at low speeds where flow separation is not present the total resistance coefficient can be written as Eq. 13[a]. Also when 0.1 < Fr < 0.2, the wave-making resistance component can be assumed to be a function of Fr^4. Then the form factor can be approximately determined as the intersected ordinate of the plot of C_T / C_F versus Fr^4 / C_F for Fr = 0 (see Eq. 13[b]). For towing speeds of U = 0.5 [m/s] Froude Number was calculated to be approximately Fr ~= 0.099 (see Eq. 14) where the form factor was measured to be around 1+k = 0.0951. Skin friction coefficient C_F^{15oC} was calculated based on Eq. 6 & 7 but with the kinematic viscosity of the water at 15 [^oC]. The R_F^{15oC} was calculated based on (Eq. 5) but with density of water ρ^{15oC} and C_F^{15oC}. The method for the calculation of the skin friction coefficient with microbubbles at 15 [^oC] $C_{F'}^{15oC}$ is same as previously mentioned. But in this case the total resistance coefficient with microbubbles at 15 [^oC] $C_{T'}^{15oC}$ could not be calculated since the Eq. 12 concerns only the case without the presence of microbubbles. To solve that it was considered that the reduction or increase rate of the resistance coefficient without microbubbles would be the same with microbubbles, $\%r_{CT} = (C_T^{15oC} - C_T) / C_T = \%r_{CT'}$. This assumption can be conducted without adding further computational error since $\%r_{CT} = (C_T + (C_F^{15oC} - C_F)\ (1 + k)$

– C_T) / C_T = (C_F^{15oC} – C_F) (1+k) / C_T = (C_F^{15oC} – C_F) (1+k) / (C_F + C_W) which is only proportional to the water's temperature T, towing speed U, but also C_W = $C_{W'}$ due to the assumption R_W = $R_{W'}$ made earlier. As a result $C_{T'}^{15oC}$ = $C_{T'}$ (1 + %r_{CT}) and $R_{T'}^{15oC}$ can be calculated by Eq. 15. In this procedure the original computational error is carried on both the net reduction of frictional resistance and frictional resistance reduction rate.

$$C_T^{15oC} = C_T + (C_F^{15oC} – C_F) (1 + k) \quad \text{(Eq. 12)}$$

$$C_T (Re, Fr) = (1 + k) C_F (Re) + C_W (Fr) \quad \text{(Eq. 13}^a\text{)}$$

$$(1 + k) = C_T / C_F \quad \text{(Eq. 13}^b\text{)}$$

$$Fr = U / (g L)^{1/2} \quad \text{(Eq. 14)}$$

$$R_{T'}^{15oC} = ½ \rho^{15oC} U^2 S C_{T'}^{15oC} \quad \text{(Eq. 15)}$$

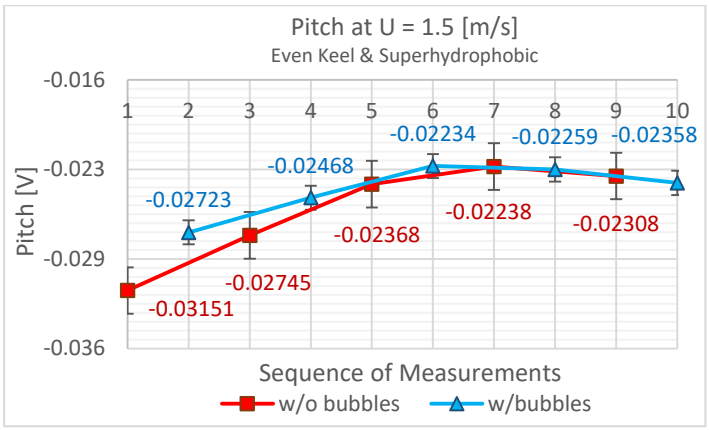

Figure 67 *Pitch at U = 1.5 [m/s] with and without microbubbles.*

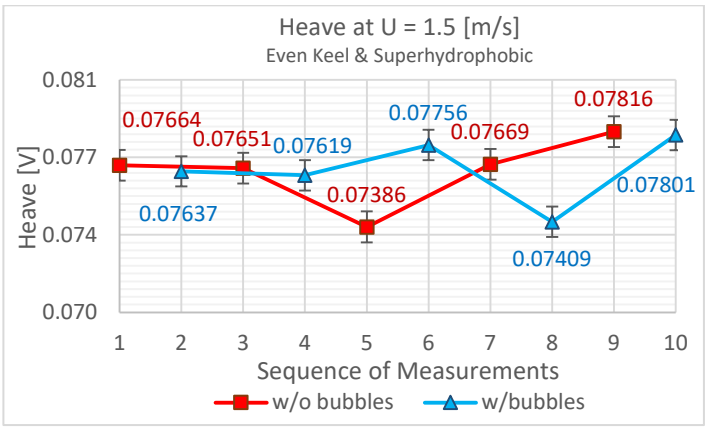

Figure 68 *Heave at U = 1.5 [m/s] with and without microbubbles.*

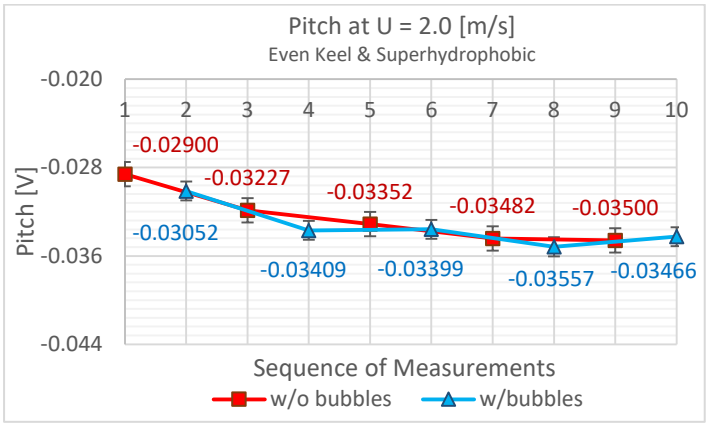

Figure 69 *Pitch at U = 2.0 [m/s] with and without microbubbles.*

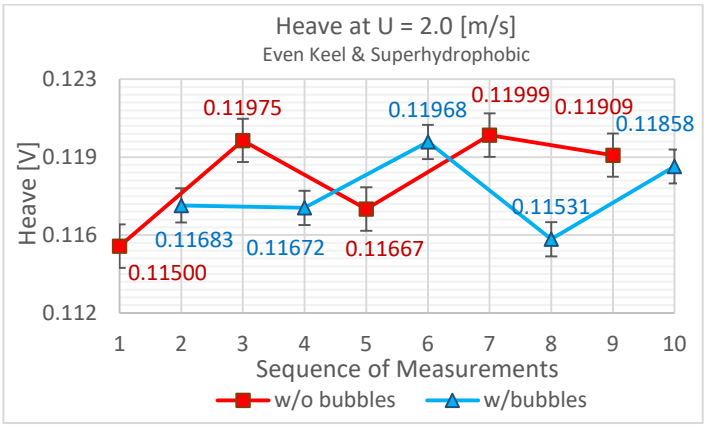

Figure 70 *Heave at U = 2.0 [m/s] with and without microbubbles.*

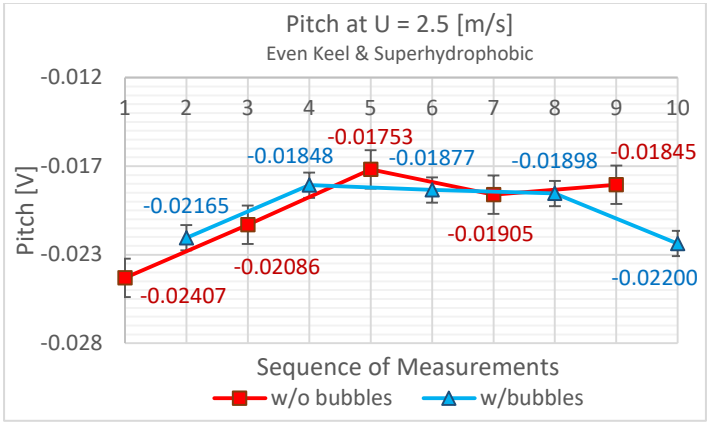

Figure 71 *Pitch at U = 2.5 [m/s] with and without microbubbles.*

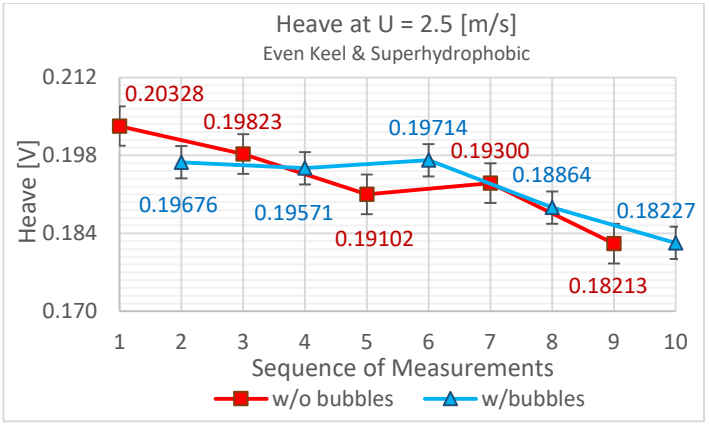

Figure 72 *Heave at U = 2.5 [m/s] with and without microbubbles.*

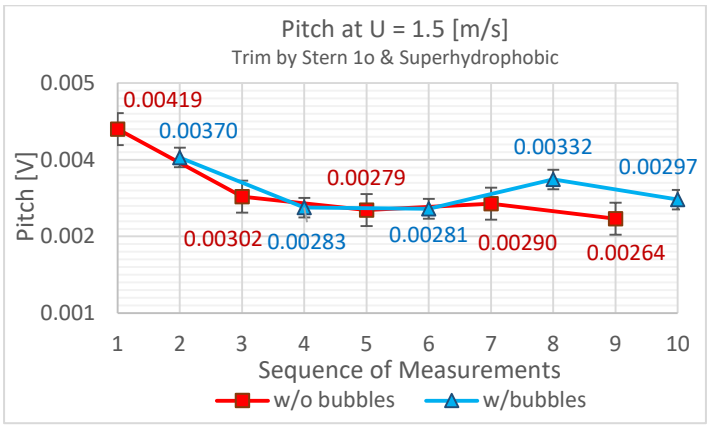

Figure 73 *Pitch at U = 1.5 [m/s] with and without microbubbles.*

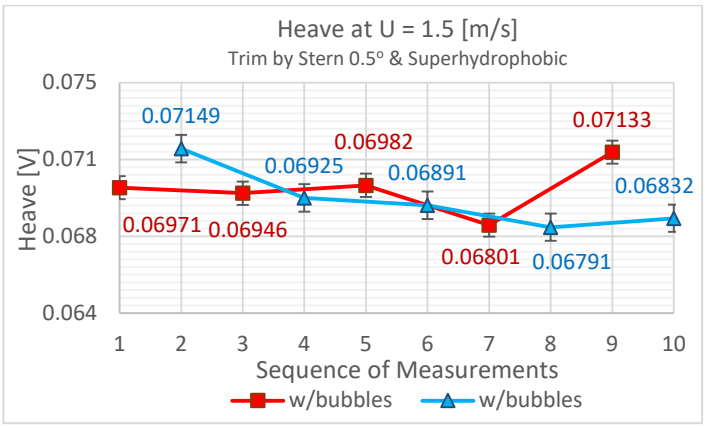

Figure 74 *Heave at U = 1.5 [m/s] with and without microbubbles.*

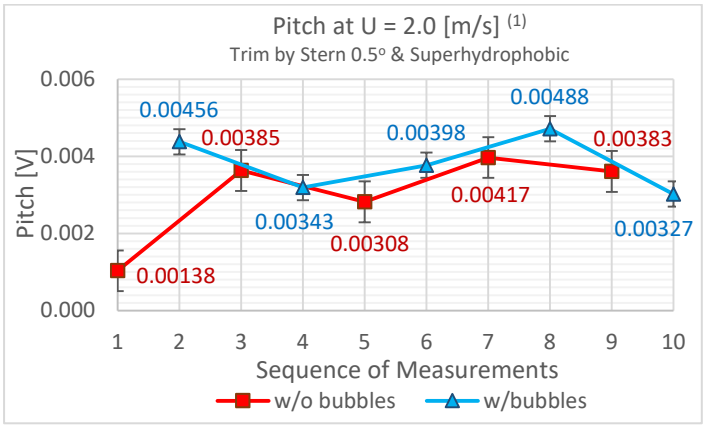

Figure 75 *Pitch at U = 2.0 [m/s] with and without microbubbles.*

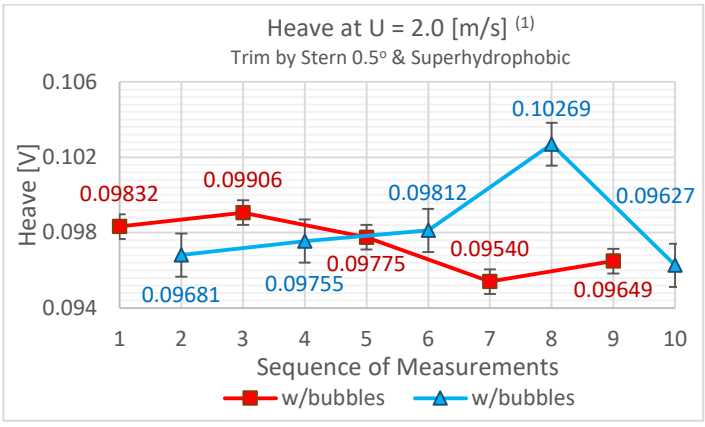

Figure 76 *Heave at U = 2.0 [m/s] with and without microbubbles.*

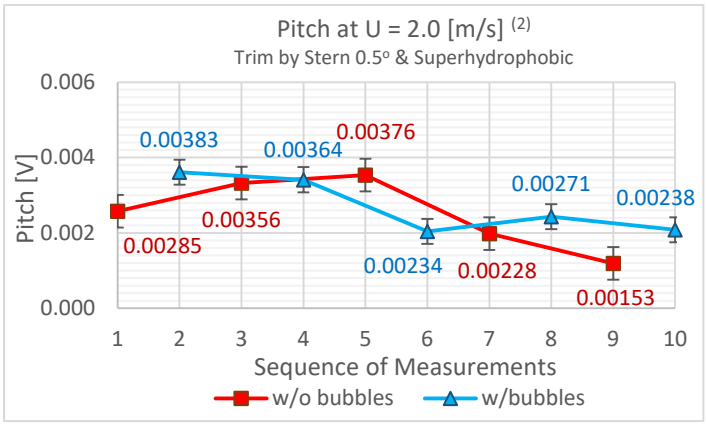

Figure 77 *Pitch at U = 2.0 [m/s] with and without microbubbles.*

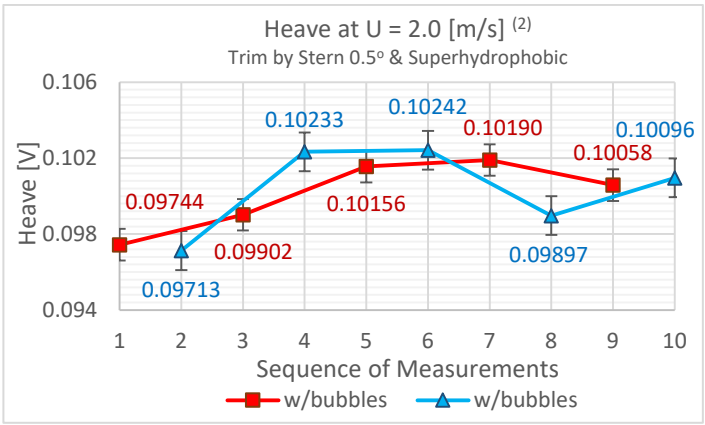

Figure 78 *Heave at U = 2.0 [m/s] with and without microbubbles.*

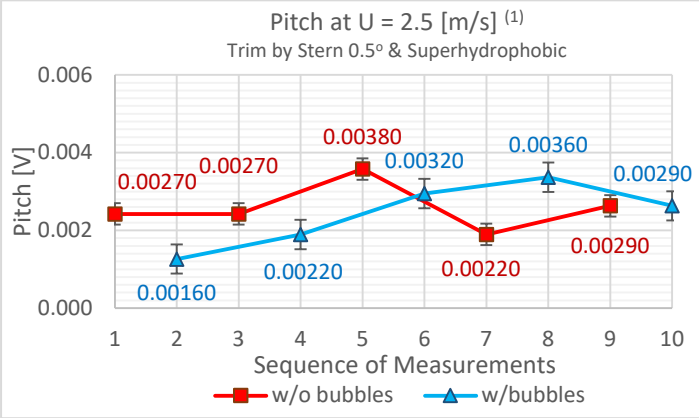

Figure 79 *Pitch at U = 2.5 [m/s] with and without microbubbles.*

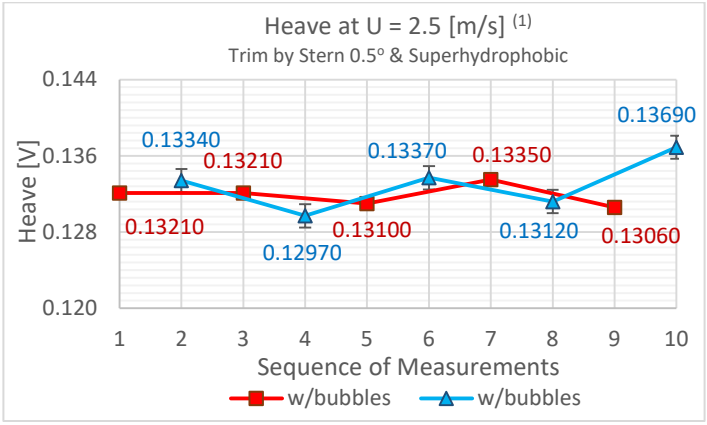

Figure 80 *Heave at U = 2.5 [m/s] with and without microbubbles.*

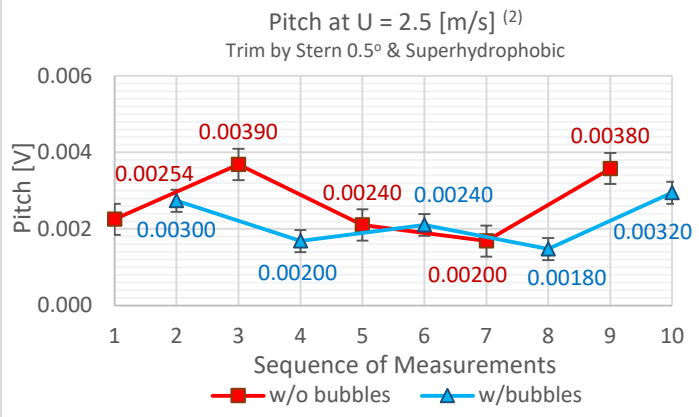

Figure 81 *Pitch at U = 2.5 [m/s] with and without microbubbles.*

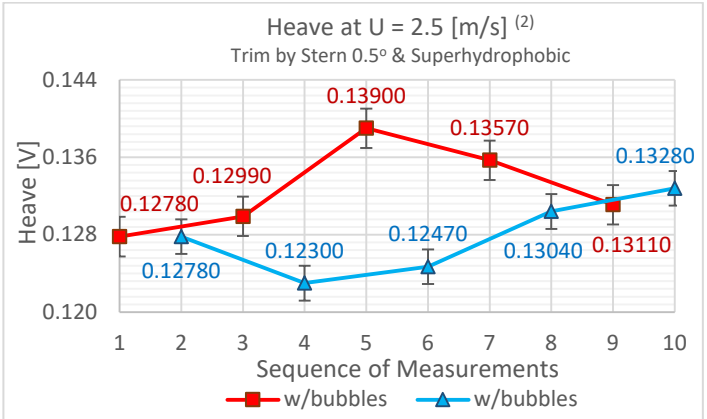

Figure 82 *Heave at U = 2.5 [m/s] with and without microbubbles.*

4.2 Experimental Results Evaluation

In this stage the previously calculated values are further analyzed in order to evaluate the reliability of the experimental procedures and accuracy of the results. For that reason the two methods of recording the experimental results were evaluated. The first method consists of a set of measurements conducted separately only for the presence or absence of microbubbles, known as exclusive-method. The second method consists of a series of measurements conducted alternately between the presence and absence of microbubbles, also known as alternating-method.

The first exclusive-method of conducting a whole series of resistance test at one specific towing speed and exclusively with or without microbubbles has its advantages and disadvantages. Aggregating multiple measurements of the same kind in one day is the biggest advantage as it provides more reliable results conducted at the most identical testing conditions (water temperature, dynamometer's transfer function etc). But two major disadvantages were noticed in this method. First, a high deviation of the measurements within two separate days was noted (see Fig. 83). Although the deviation between the average of Day A and Day B ranges to 0.35% since we are expecting a drag reduction of around more than 1% a 1/3 of uncertainty drives serious problem in the analysis of measurements and precise evaluation of the effect of microbubbles for frictional drag reduction. It is also worth mentioning that the net difference between Day A and Day B is $\Delta R_{T\_A\&B}$ = 0.0661 [N] = 0.00674 [kp] and approximately 6.74 [g] which is above dynamometer's minimum accuracy of 5 [g]. It should also be mentioned that the temperature of Day A was 13.2 [^{o}C] and Day B was 13.5 [^{o}C] and both measurements were converted into the nominal temperature of 15 [^{o}C]. Secondly, an unexpected deviation was noted throughout the measurements of the same day approximately 2.46 [g] between the minimum and maximum recorded resistance (see Fig. 84). As it can be seen from the sequence of measurements a declining and increasing area can be noted instead of following a random deviation due to calibration errors. It should be mentioned that in between each run a dead time of 15 [min] were given, meaning that the 1st measurement has more than 1 hour and a half hour difference from the last 8th measurement. Since most measurements were conducted at around 10 am heading towards the noon the temperature of the water should have been slightly increasing leading to the decrease of the density of water and as a result to less total resistance. But the opposite pattern indicates that other factors than temperature itself were present and affecting the testing results. One of them would be the factor of residual energy within the towing tank accumulated with each run. Regardless of the given dead time the maintenance of the same condition is almost impossible and the addition of energy with each run would have created a complex flow of energy underneath the free surface. Also the unpredictable deviation of the dynamometer should come into play as well as the electrical outputs could have carried varying residual electrical signals of its circuit.

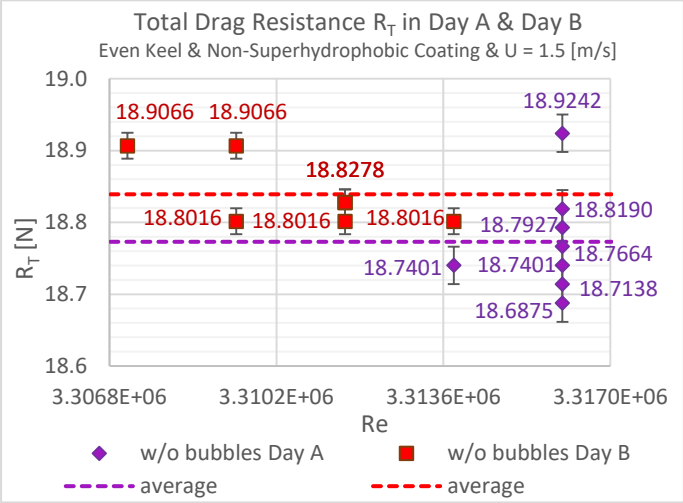

Figure 83 *Deviation of total resistance R_T between Day A and Day B.*

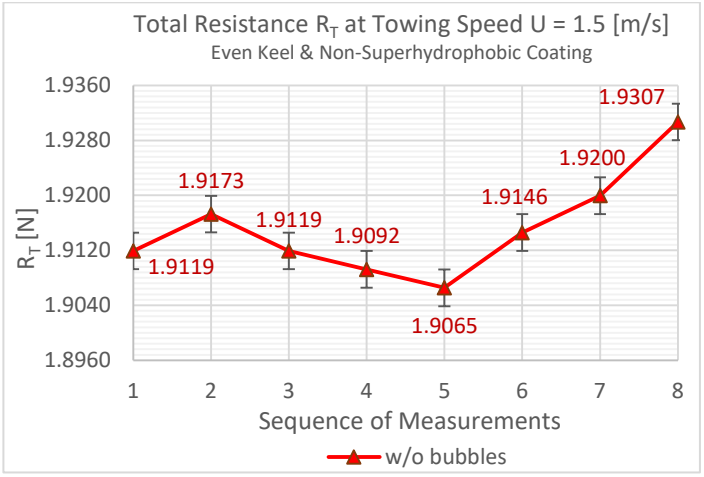

Figure 84 *Deviation of total resistance R_T within a series of measurements.*

The second alternating-method of conducting a whole series of resistance test at one specific towing speed and alternating between the absence and presence of microbubbles was found to be more optimal and eliminate the disadvantages of the prior method. But it should be mentioned that this method must follow an exact alternating between the condition with and without microbubbles rather than following a random sequence of measurements. This is crucial since the purpose of this method is to conduct two different conditions (with and without microbubbles) in the closest and identical testing condition without the interference of unknown external factors (change of temperature, dynamometer's calibration, residual energy within the tank etc.). A series of test conducted with a random alternation with and without the presence of microbubbles is presented in Fig. 85. As it was mentioned in Fig. 84 a pronounced high and low areas are present regardless of the presence or not of the microbubbles indicating the need of conducting the measurements with the least time difference and exact alternating. Based on this method the total resistance with and without microbubbles were recorded (see Fig. 86-89). It is worth noting that each resistance test has a unique deviation a pattern of which is almost identical for both resistances with and without microbubbles. Also it can be noted that at lower towing speeds the resistances with and without microbubbles may intersect while at higher speeds the deviation between the two conditions are more pronounced. Also along each representation of the total resistance the initial voltage of the dynamometer at quiescent condition measured before each run is also presented. Comparing both the total resistance with the initial voltage no correlation can be found indicating that the pattern of the measurements is not depended on the uncertainty of the electrical circuit.

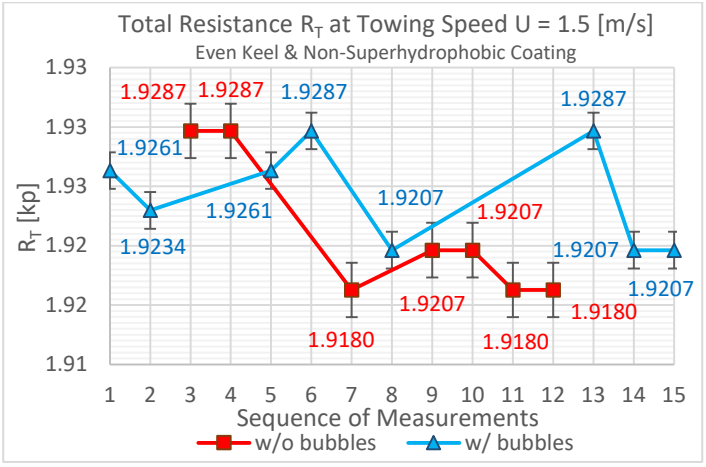

Figure 85 *Measurements deviation throughout the series of test due to unknown uncertainties.*

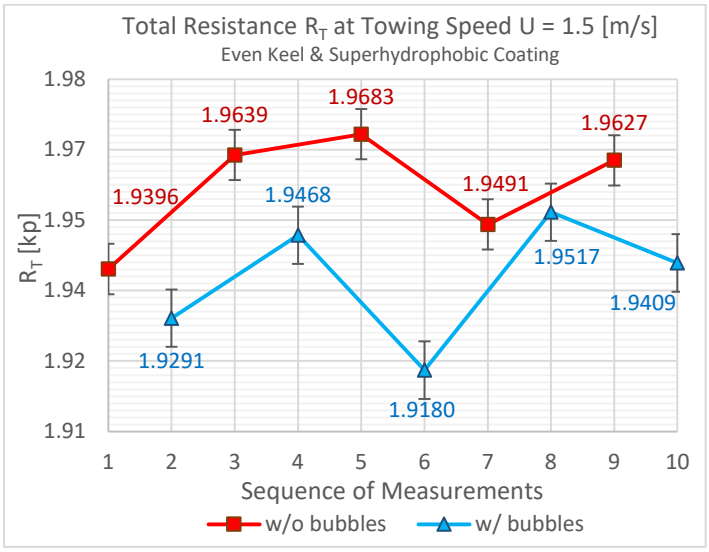

Figure 74 *Total resistance measured in a one-after-the-other sequence.*

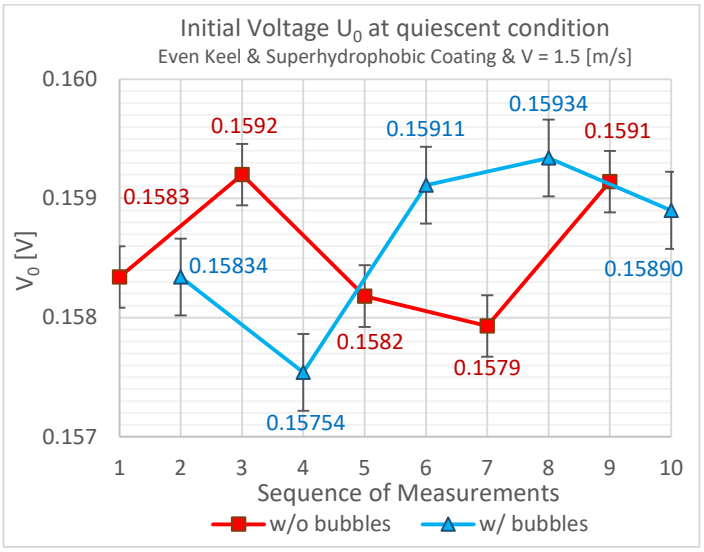

Figure 75 *Initial Voltage of the dynamometer measured in a one-after-the-other sequence.*

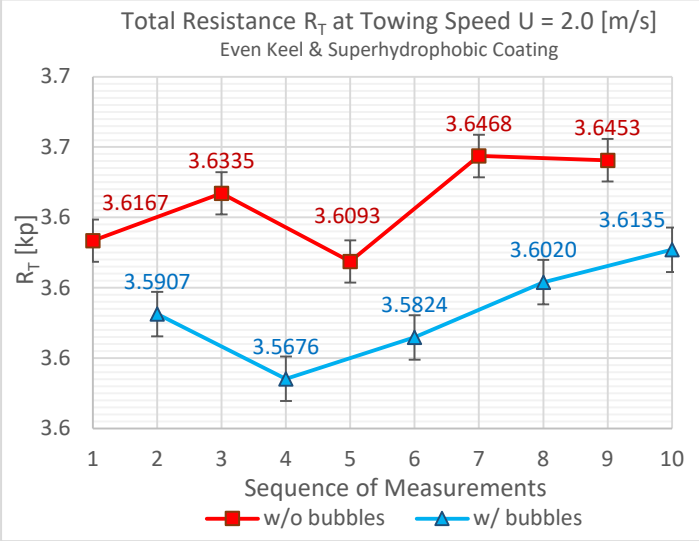

Figure 76 *Total resistance measured in a one-after-the-other sequence.*

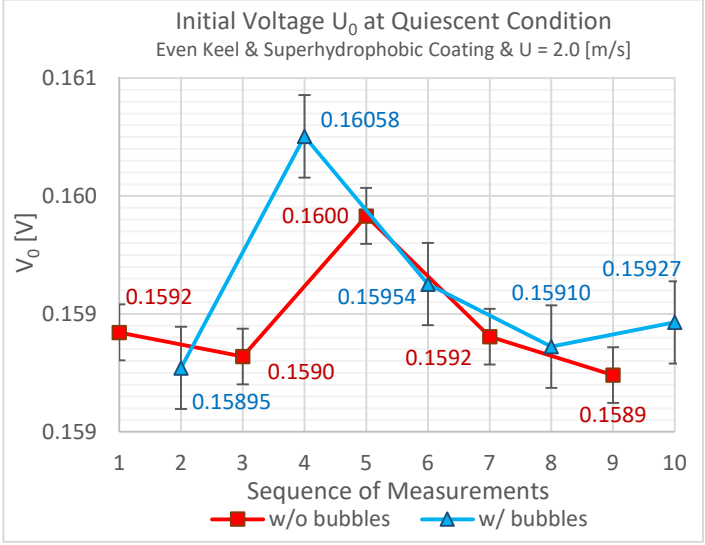

Figure 77 *Initial Voltage of the dynamometer measured in a one-after-the-other sequence.*

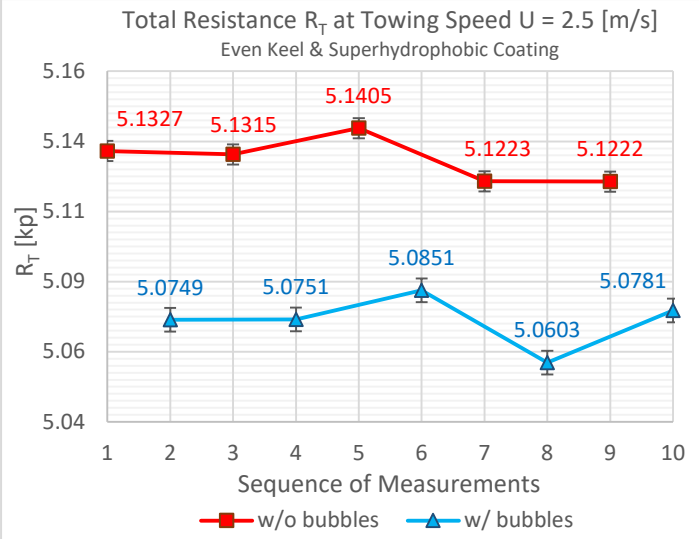

Figure 78 *Total resistance measured in a one-after-the-other sequence.*

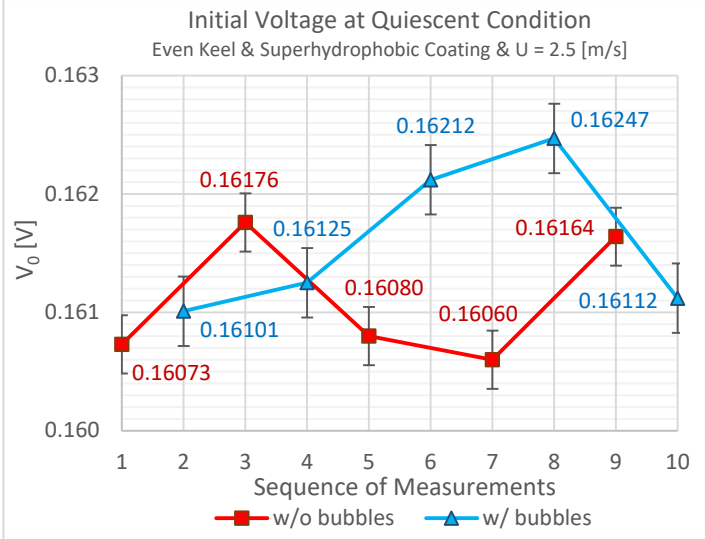

Figure 79 *Initial Voltage of the dynamometer measured in a one-after-the-other sequence.*

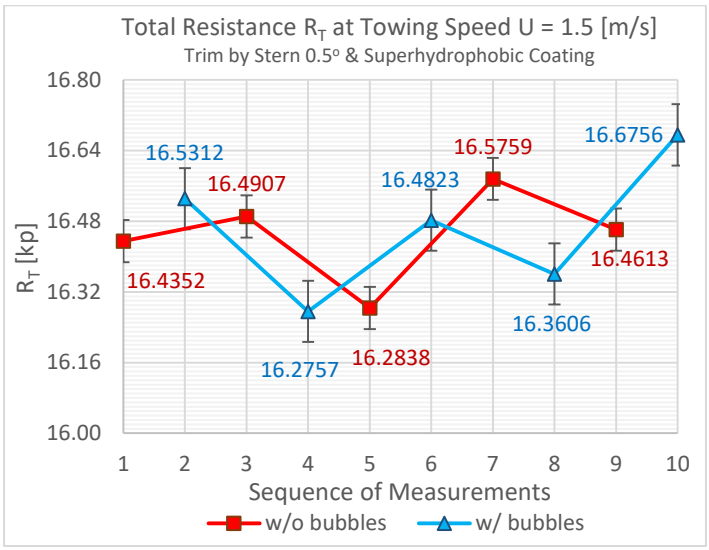

Figure 80 *Total resistance measured in a one-after-the-other sequence.*

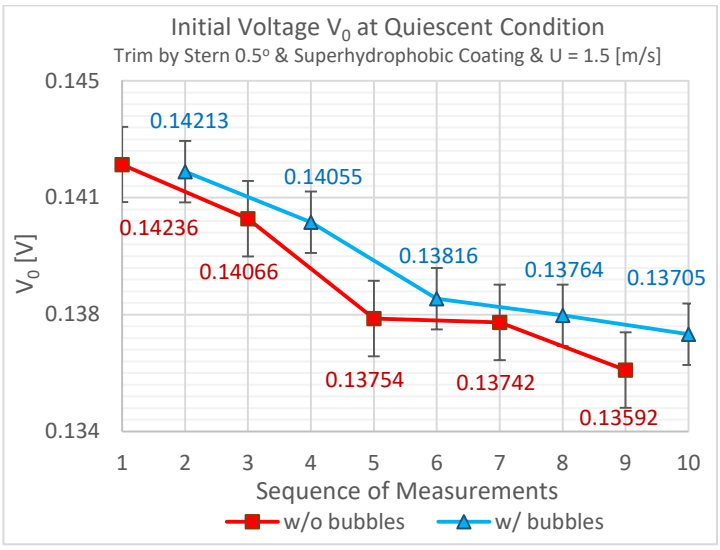

Figure 81 *Initial Voltage of the dynamometer measured in a one-after-the-other sequence.*

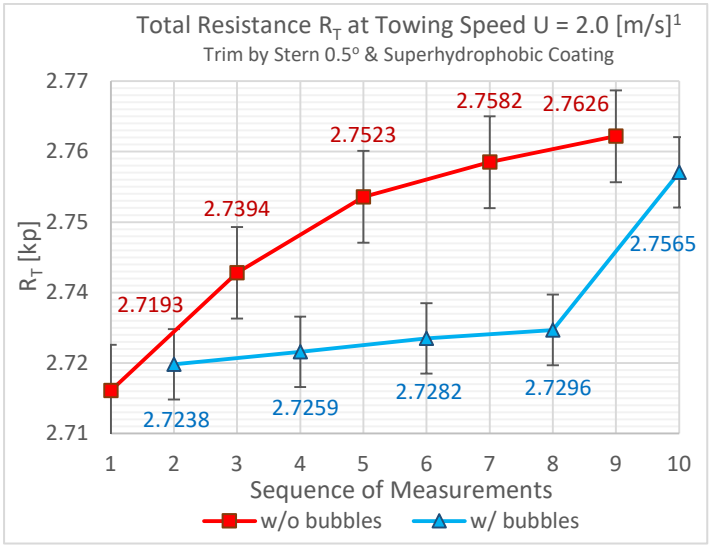

Figure 82 *Total resistance measured in a one-after-the-other sequence.*

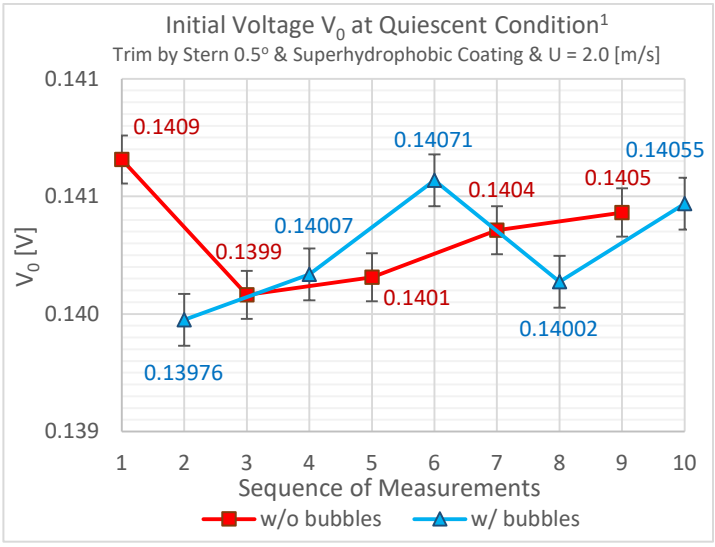

Figure 83 *Initial Voltage of the dynamometer measured in a one-after-the-other sequence.*

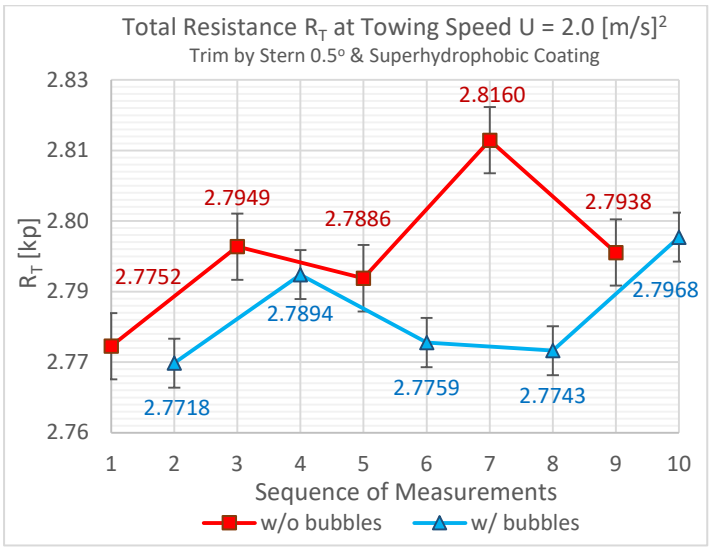

Figure 84 *Total resistance measured in a one-after-the-other sequence.*

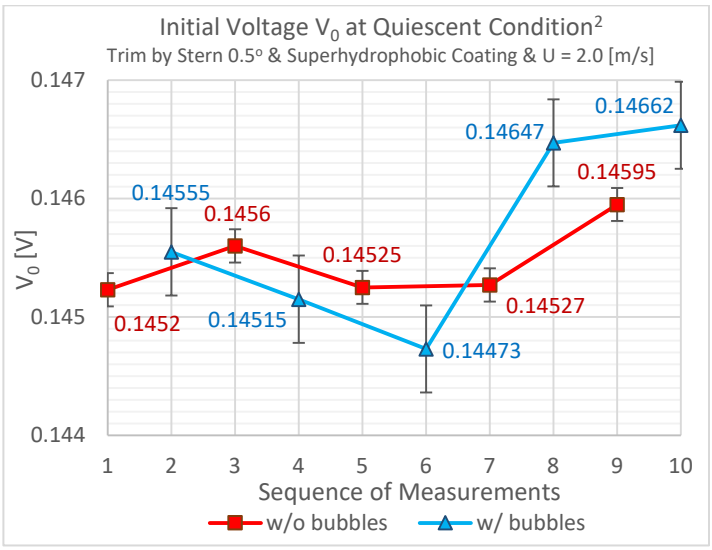

Figure 85 *Initial Voltage of the dynamometer measured in a one-after-the-other sequence.*

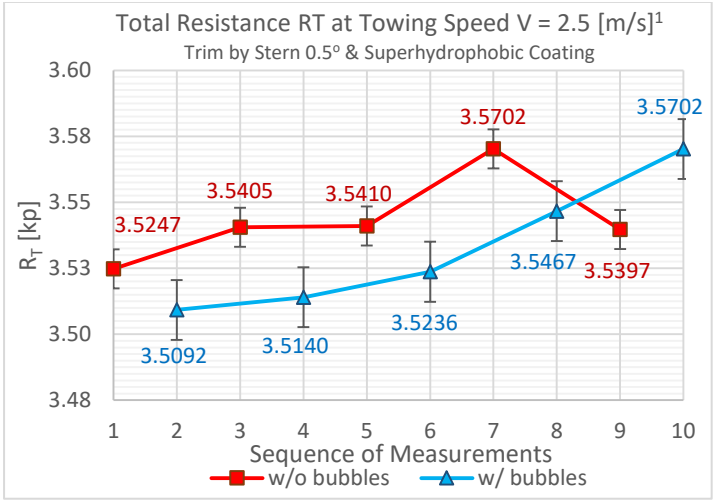

Figure 86 *Total resistance measured in a one-after-the-other sequence.*

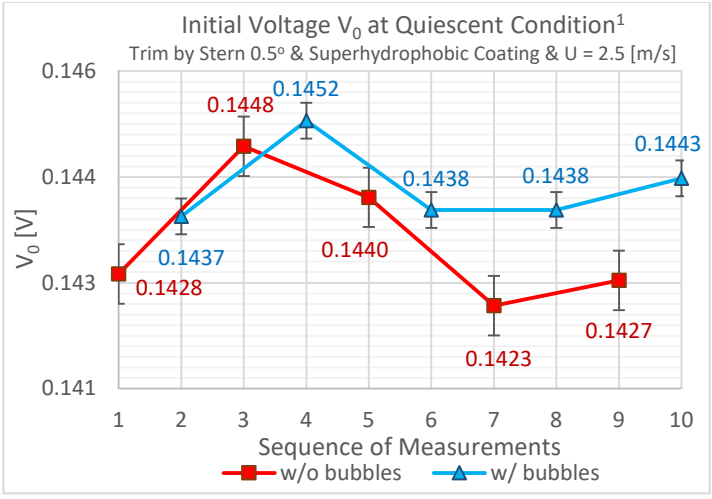

Figure 87 *Initial Voltage of the dynamometer measured in a one-after-the-other sequence.*

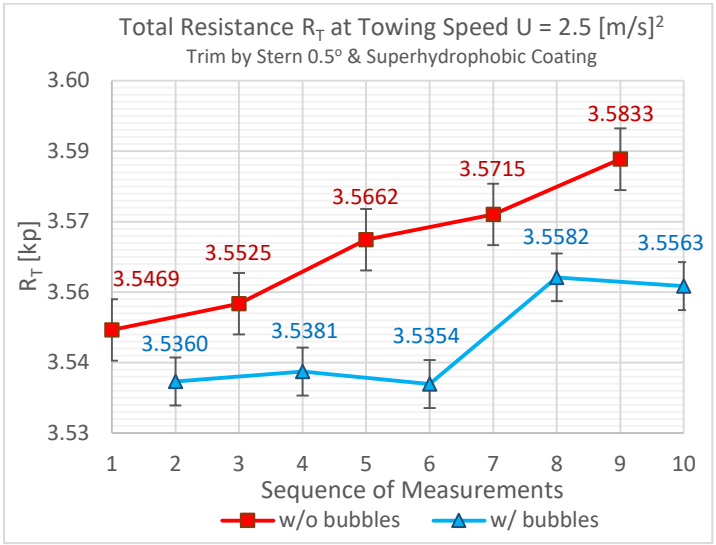

Figure 88 *Total resistance measured in a one-after-the-other sequence.*

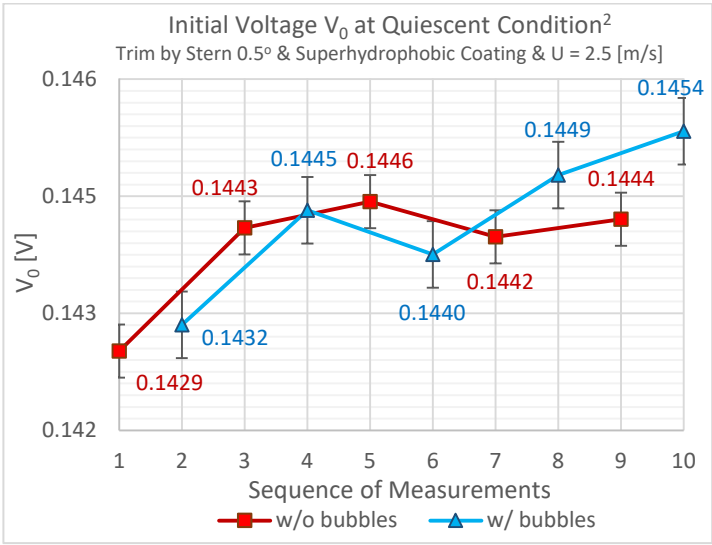

Figure 89 *Initial Voltage of the dynamometer measured in a one-after-the-other sequence.*

4.3 Experimental Results Interpretation

The results of the measurements taken under the right method are presented and the effect of microbubbles in the reduction of frictional drag is interpreted. At even keel an average reduction of 1.0483% and 4.0796% was noted for R_T and C_F respectively (see Tb. 3). At trim by stern 0.5° an average reduction of 0.4239% and 1.2821% was noted for R_T and C_F respectively (see Tb. 4). The average of total resistance R_T with and without the introduction of microbubbles are compared (see Fig. 90 & 91). Specifically in all towing speeds and hydrodynamic conditions (even keel, trim by stern 0.5°) a reduction of frictional drag was noted. It should be mentioned that all the below values are converted for the nominal temperature 15 [°C].

Table 3 *Average of total resistance with and without microbubbles at even keel.*

Towing Speed	Total Resistance			Skin Friction Coefficient		
U [m/s]	R_T [N]	$R_{T'}$ [N]	$\%r_{RT}$	C_F	$C_{F'}$	$\%r_{CF}$
1.5	19.2143	19.0237	-0.9919%	0.003674	0.003538	-3.6800%
2.0	35.6192	35.2353	-1.0777%	0.003478	0.003321	-4.5098%
2.5	50.3823	49.8405	-1.0753%	0.003336	0.003201	-4.0492%
	$\%r_{RT\_average}$ =		**-1.0483%**	$\%r_{CF\_average}$ =		**-4.0797%**

Table 4 *Average of total resistance with and without microbubbles at trim by stern 0.5°.*

Towing Speed	Total Resistance			Skin Friction Coefficient		
U [m/s]	R_T [N]	$R_{T'}$ [N]	$\%r_{RT}$	C_F	$C_{F'}$	$\%r_{CF}$
1.5	16.4687	16.4187	-0.3035%	0.003674	0.003638	-0.9871%
2.0	27.1875	27.0383	-0.5491%	0.003477	0.003417	-1.7344%
2.5	34.9060	34.7596	-0.4192%	0.003336	0.003299	-1.1229%
	$\%r_{RT\_average}$ =		**-0.4239%**	$\%r_{CF\_average}$ =		**-1.2815%**

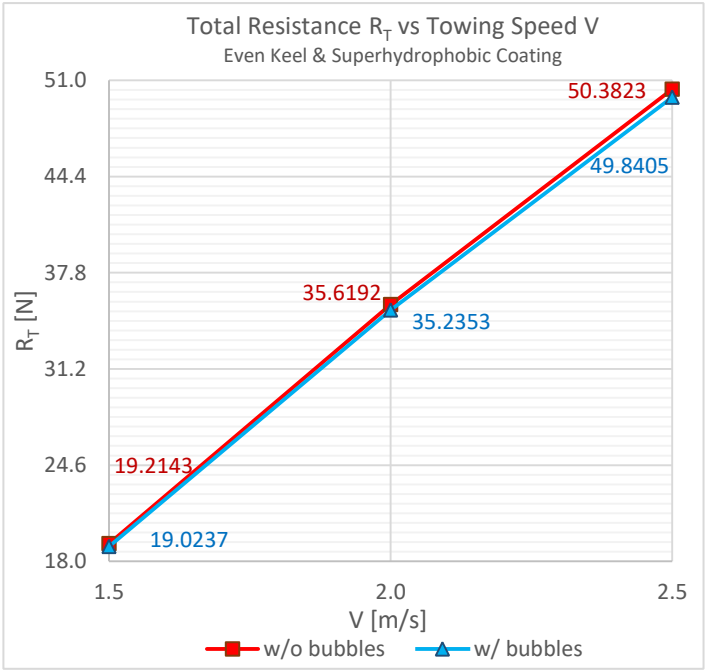

Figure 90 *Average of total resistance with and without microbubbles on even keel and superhydrophobic coating.*

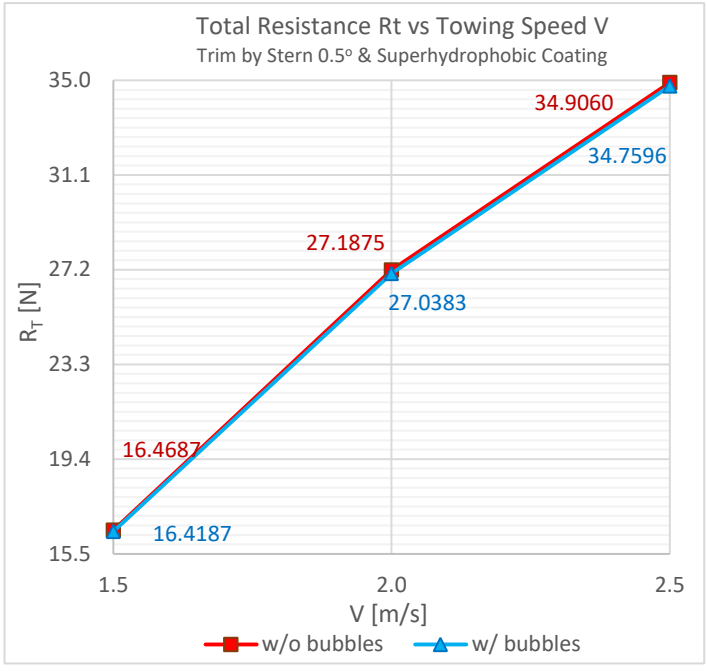

Figure 92 *Average of total resistance with and without microbubbles on trim by stern 0.5° and superhydrophobic coating.*

The above measurements are presented for each individual towing speed and hydrodynamic condition (see Fig. 93-98). When comparing each distinct total resistance points for towing speeds 1.5, 2.0, and 2.5 [m/s] a notable increase of the discrepancy between the average resistances with and without the microbubbles can be noted. For lower speeds the discrepancy between the two conditions (with and without microbubbles) is small as the measured resistances fall closer to the measurement error (see Fig. 93 the area where resistance values for the two conditions are collapsed) but also due to the fact that the percentage reduction for smaller values are proportionally smaller. Although more drag reduction was expected to be noted at lower speeds where wave making components are far more less than at higher speeds, these results indicate the effect of the microbubbles does not depend on the wave resistance but exclusively to the frictional resistance. Another important result from the measurements is the decrease of the drag reduction when the ship model was towed with trim by stern 0.5^{o}. Although a more pronounced reduction was expected with trim the opposite is observed.

This indicates with trim by stern although the microbubbles attach on the wetted surface of flat of bottom the free flow also migrates the microbubbles away from the surface as it constantly meets the surface at an angle.

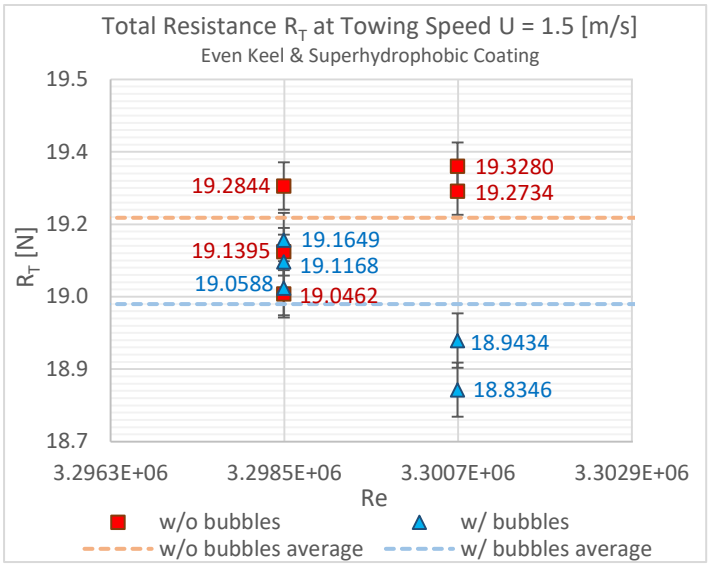

Figure 93 *Total Resistance with and without microbubbles at towing speed U = 1.5 [m/s] on even keel and superhydrophobic coating.*

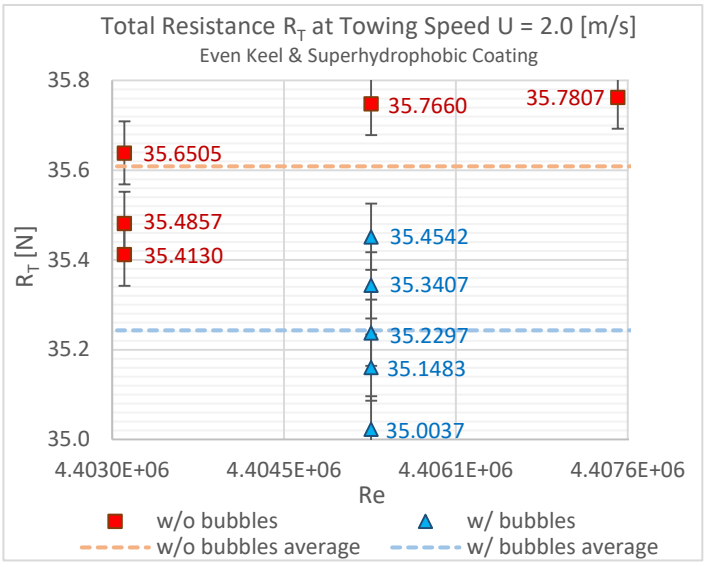

Figure 94 *Total resistance with and without microbubbles at towing speed U = 2.0 [m/s] on even keel and superhydrophobic coating.*

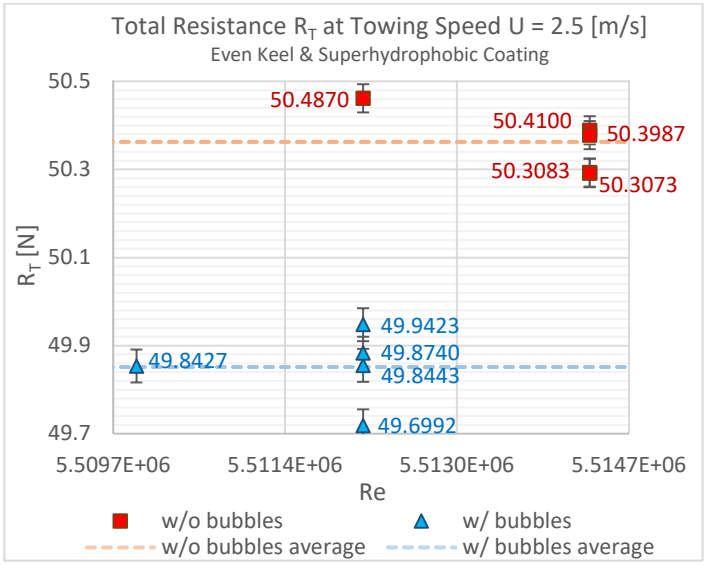

Figure 95 *Total resistance with and without microbubbles at towing speed U = 2.5 [m/s] on even keel and superhydrophobic coating.*

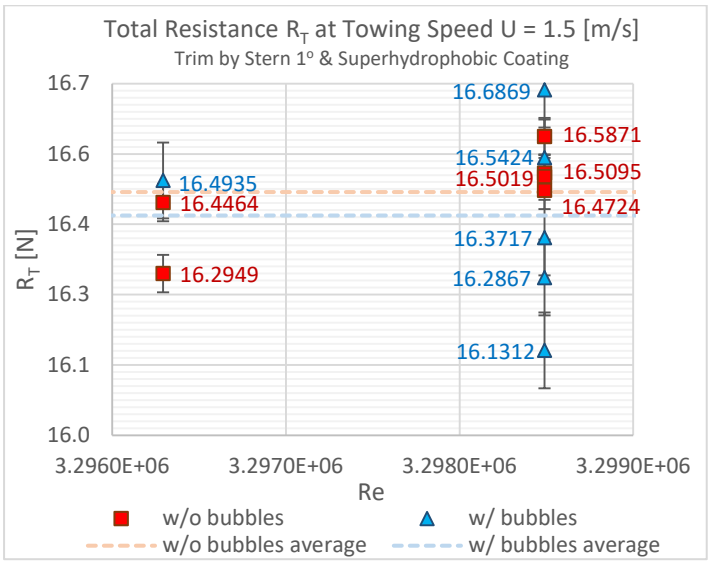

Figure 96 *Total resistance with and without microbubbles at towing speed U = 1.5 [m/s] on trim by stern 0.5º and superhydrophobic coating.*

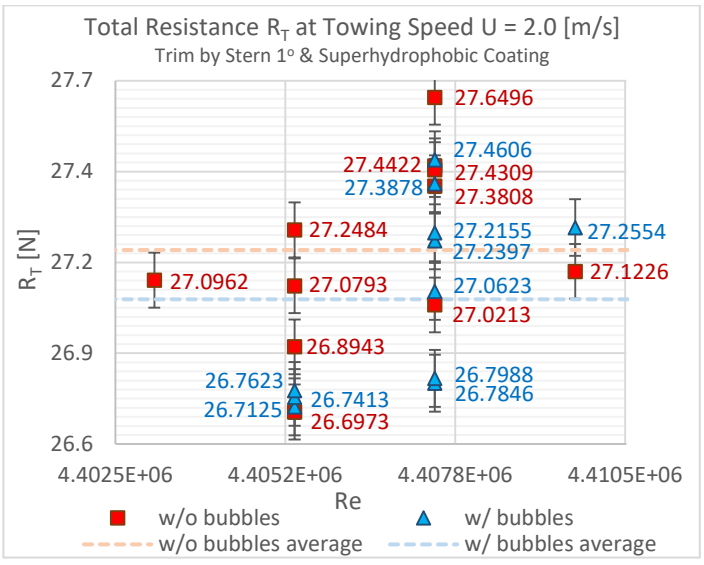

Figure 97 *Total resistance with and without microbubbles at towing speed U = 2.0 [m/s] on trim by stern 0.5º and superhydrophobic coating.*

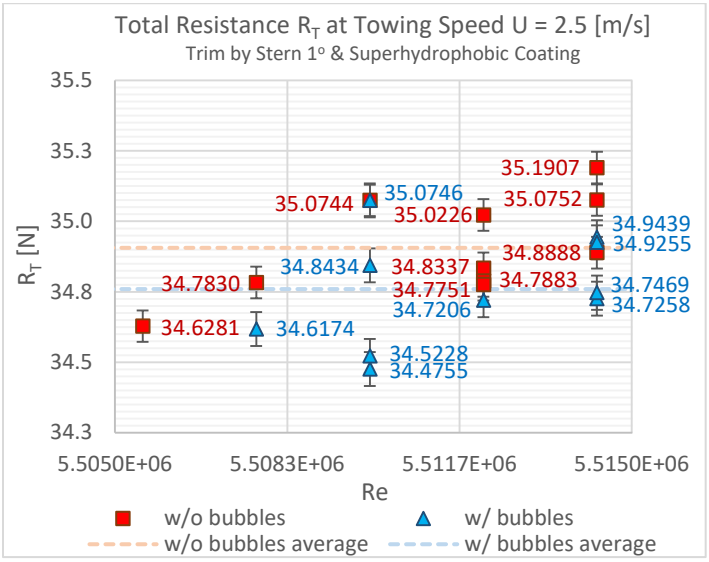

Figure 98 *Total resistance with and without microbubbles at towing speed U = 2.5 [m/s] on trim by stern 0.5º and superhydrophobic coating.*

When skin friction coefficient was plotted against the towing speeds an interesting result was extracted (see fig. 99-101). Although a reduction of skin friction coefficient was found at all speeds the maximum reduction was found at U = 2.0 [m/s], indicating that there is an optimal speed where the effect of the microbubble is maximized as it was found in previous literature (see Literature Review). In other words, since the flow rate of the microbubbles was constant at all testing conditions and only the thickness of the boundary layer would change with the change of the towing speeds. More specifically, the boundary layer would become thinner the higher the towing speed. Thus it can be conjectured that at U = 2.0 [m/s] the microbubble are effectively diffused in the buffer layer where most turbulence occurs as previous literatures suggest. This also indicates that for each distinct microbubble flow rate, there is an optimal towing speed. For more effective manipulation the effect of frictional drag reduction with microbubbles the microbubble generating system should be able to produce this lubrication at varying rates. Finally, it can be deduced that the microbubble lubricating technique and the superhydrophobic technique are not correlated. The notable increase in total resistance when plotted against the sequence of measurements indicate that for every towing test shear force of the flow gradually removes bubbles attached on the superhydrophobic coating (see Fig. 74, 76, 78, 80, 82, 84, 8, 88). These bubbles are not due to the microbubble generated by the CARMIN D1s but rather due to its unique nano-ceramic roughness. In other words, the superhydrophobicity seems to effect the surface-liquid interface alone, while the microbubble generated by the CARMIN D1s seem to effect the viscosity and turbulence reduction of the flow.

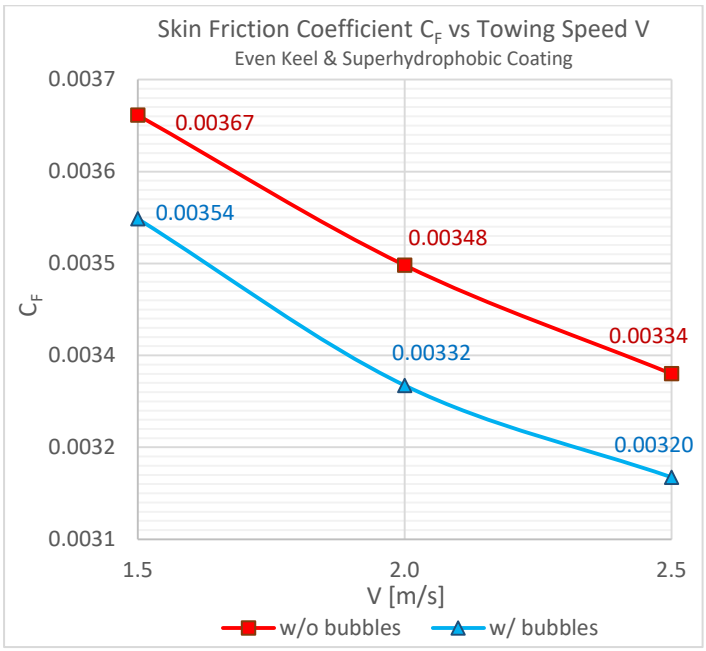

Figure 99 *Average of total skin friction coefficient with and without microbubbles on even keel and superhydrophobic coating.*

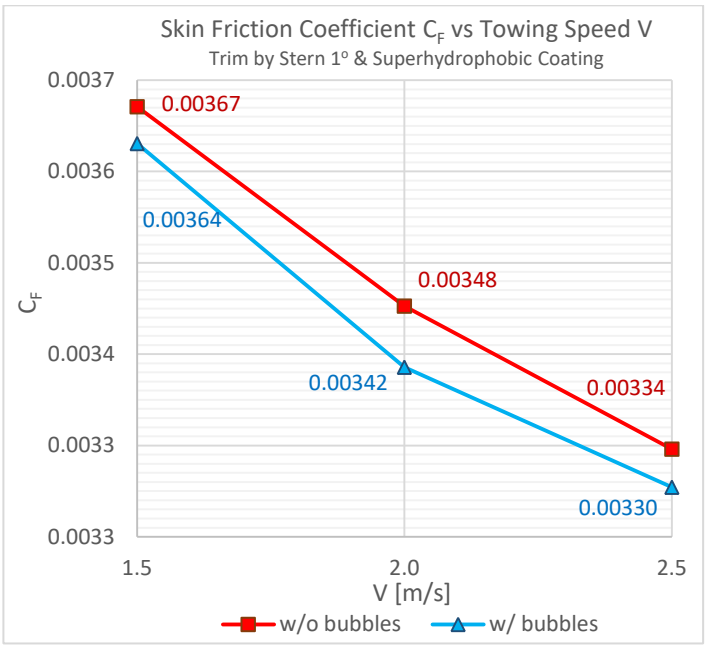

Figure 100 *Average of total skin friction coefficient with and without microbubbles on trim by stern 0.5° and superhydrophobic coating.*

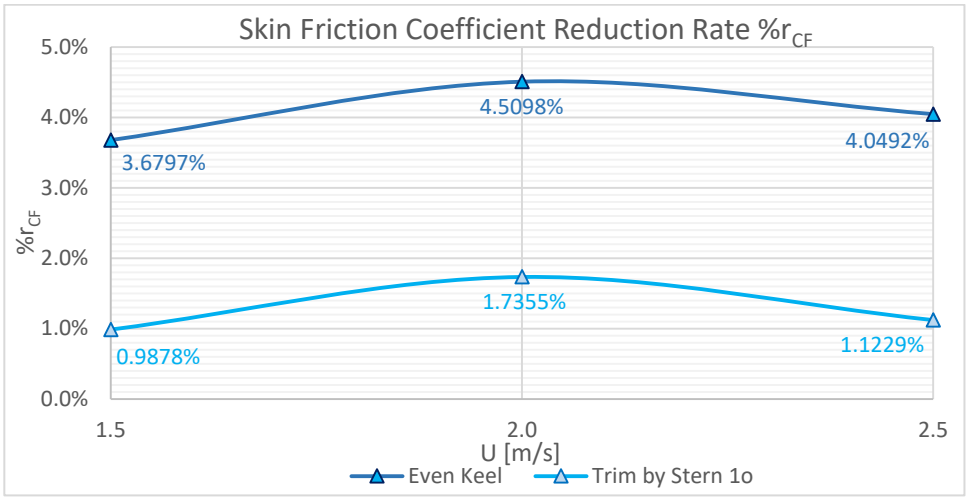

Figure 94 *Skin friction coefficient reduction rate at even keel and trim by stern 0.5°.*

REFERENCES

Bhattacharrya, R., & McCormick, M. E. (1973). Nav. Eng. J. *85*, 11.

Crewe, P. R., & Eggington, W. J. (1960). Trans. Roy. Inst. Nav. Arch. *102*, 315.

Gutierrez-Torres, Y. A. (2006). Investigation of Drag Reduction Mechanism by Microbubble Injection within a Channel Boundary Layer Using Particle Tracking Velocimetry.

Jacob, B., Olivieri, A., Miozzi, M., Campana, E. F., & Piva, R. (2010). Drag reduction by microbubbles in a turbulent boundary layer. *Physics of Fuilds, 22*.

Lumley, J. L. (1964). "The Reduction of Skin Friction Drag". *Fifth Office of Naval Research Symposium on Naval Hydrodynamics.* Bergen, Norway.

Madavan, N. K., Deutsch, S., & Merkle, C. L. (1984a). Reduction of turbulent skin friction by microbubbles. *Phys. Fluids, 27*, 356-363.

Madavan, N. K., Deutsch, S., & Merkle, C. L. (1984b). The effect of porous material on microbubble skin friction reduction. *AIAA 84-0348*.

Madavan, N. K., Deutsch, S., & Merkle, C. L. (1985). Measurements of local skin friction in a microbubble modified turbulent boundary layer. *Journal of Fluid Mechanics, 156*, 237-256.

Molland, A., Turnock, S., & Hudson, D. (2017). *Components of Hull Resistance.* Cambridge University Press. Retrieved from Cambridge University Press.

Paik, B. G., Yim, G. T., Kim, K. Y., & Kim, K. S. (2016). The effects of microbubbles on skin friction in a turbulent boundary layer flow. *International Journal of Multiphase Flow, 80*, 164-175.

Report of the Marine Environment Protection Committee on its Fifty-Eighth Session. (2008).

Rothenstein, JP. (2010). Slip on superhydrophobic surfaces. *Annual review of fluid mechanics*.

Sanders, W. C., Winkel, E. W., Dowling, D. R., Perlin, M., & Ceccio, S. L. (2006). Bubble friction drag reduction in a high Reynolds number flat plate turbulent boundary layer. *J Fuild Mech, 552*, 353-380.

Schlichting, H., & Gersten, K. (1960). *Boundary Layer Theory.* Springer, Berlin, Heidelberg.

Watanabe, M. (1991). Air pollution from ship engines in maritime transport. *Mar Eng Soc Jpn, 26*(9).